Stochastic Forcing of ENSO by the Intraseasonal Oscillation

ANDREW M. MOORE

Program in Atmospheric and Oceanic Sciences and Cooperative Institute for Research in Environmental Sciences, University of Colorado, Boulder, Colorado

RICHARD KLEEMAN

Bureau of Meteorology Research Centre, Melbourne, Victoria, Australia

(Manuscript received 26 August 1997, in final form 10 March 1998)

ABSTRACT

Using the ideas of generalized linear stability theory, the authors examine the potential role that tropical variability on synoptic–intraseasonal timescales can play in controlling variability on seasonal–interannual timescales. These ideas are investigated using an intermediate coupled ocean–atmosphere model of the El Niño–Southern Oscillation (ENSO). The variability on synoptic–intraseasonal timescales is treated as stochastic noise that acts as a forcing function for variability at ENSO timescales. The spatial structure is computed that the stochastic noise forcing must have in order to enhance the variability of the system on seasonal–interannual timescales. These structures are the so-called stochastic optimals of the coupled system, and they bear a good resemblence to variability that is observed in the real atmosphere on synoptic and intraseasonal timescales. When the coupled model is subjected to a stochastic noise forcing composed of the stochastic optimals, variability on seasonal–interannual timescales develops that has spectral characteristics qualitatively similar to those seen in nature. The stochastic noise forcing produces perturbations in the system that can grow rapidly. The response of the system to the stochastic optimals is to induce perturbations that bear a strong resemblence to westerly and easterly wind bursts frequently observed in the western tropical Pacific. In the model, these ''wind bursts'' can act as efficient precursors for ENSO episodes if conditions are favorable. The response of the system to noise-induced perturbations depends on a number of factors that include 1) the phase of the seasonal cycle, 2) the presence of nonlinearities in the system, 3) the past history of the stochastic noise forcing and its integrated effect, and 4) the stability of the coupled ocean–atmosphere system. Based on their findings, they concur with the view adopted by other investigators that ENSO may be explained, at least partially, as a stochastically forced phenomena, the source of the noise in the Tropics being synoptic–intraseasonal variability, which includes the Madden–Julian oscillation, and westerly/easterly wind bursts. These ideas fit well with the observed onset and development of various ENSO episodes, including the 1997–98 El Niño event.

1. Introduction

Through coordinated observation and numerical modeling efforts, the recent Tropical Ocean Global Atmosphere (TOGA) experiment has revealed a great deal about air–sea interaction in the Tropics, leading to an increased understanding of the El Niño–Southern Oscillation phenomenon (ENSO) (National Research Council 1996). While a number of competing theories and mechanisms proposed for ENSO episodes exist (see reviews by McCreary and Anderson 1991; Neelin et al. 1994; Battisti and Sarachik 1995), there is fairly strong observational and modeling evidence (Mantua and Battisti 1994; Boulanger and Fu 1996) to support the idea that ENSO is, by and large, governed by a delayed-action oscillator, an idea originally proposed by McCreary (1983), and later modified by Suarez and Schopf (1988) and Battisti and Hirst (1989). However, observations reveal that no two ENSO episodes are completely alike, and, in fact, the episodes of the 1990s are quite different from those of the 1970s and 1980s. This perhaps suggests that no single mechanism is solely responsible for ENSO, and that the relative importance of different physical processes may vary from episode to episode.

Despite its name, it is debatable whether ENSO is really an oscillation, since individual events tend to be episodic rather than part of a regular oscillatory cycle. Fourier spectra of the NINO3 index (the sea surface temperature anomaly averaged over the central and eastern tropical Pacific, 5°N–5°S, 90°–150°W) and the Southern Oscillation index (SOI) reveal a rather broad spectral maximum centered around a period just shy of

Corresponding author address: Dr. Andrew M. Moore, Program in Atmospheric and Oceanic Sciences, CIRES, University of Colorado, Campus Box 311, Boulder, CO 80309-0311.
E-mail: andy@australis.colorado.edu

4 yr (Blanke et al. 1997; Kestin et al. 1998). In recent times, the period between episodes has been quite irregular, varying between 2–10 yr. Historical records also reveal that there have been periods in the past when there was little or no ENSO activity, such as the 1920s and 1930s (Torrence and Webster 1998).

While the development of established ENSO episodes is thought to be reasonably well understood, there is still much debate about the cause of the irregularity in the occurrence of episodes, and the observed decadal variations in ENSO activity. One idea currently abroad is that such irregularities and variability is due to a modulation of the tropical Pacific Ocean circulation by extratropical effects, both near-surface effects with timescales of a few years, and deep ocean effects on longer timescales associated with changes in the thermohaline circulation of the ocean (McCreary and Lu 1994; Liu et al. 1994; Gu and Philander 1997; Gray and Sheaffer 1997). Another popular idea gaining momentum builds on ideas proposed by Hasselmann (1976) and is that high-frequency transients in the atmosphere and ocean can act as an effective stochastic forcing for the coupled system, causing ENSO episodes to occur aperiodically (Lau 1985; Lau and Chan 1986, 1988; Schopf and Suarez 1988; Battisti 1988; Vallis 1988; Zebiak 1989; Penland and Matrasova 1994; Penland and Sardeshmukh 1995; Penland 1996; Wainer and Webster 1996; Kleeman and Moore 1997; Blanke et al. 1997; Eckert and Latif 1997). Other studies have sought to explain ENSO as a chaotic phenomenon involving interactions between ENSO and the seasonal cycle (Zebiak and Cane 1991; Munnich et al. 1991; Jin et al. 1994, 1996; Chang et al. 1994, Tziperman et al. 1994, 1995, 1997).

In this paper we revisit the idea that ENSO episodes are a stochastically forced phenomena, under the basic premise that tropical variability on seasonal–interannual timescales is distinct from variability on synoptic–intraseasonal timescales. This is a reasonable assumption since spectra of the observed variability in the Tropics do show a fairly pronounced spectral gap between these two timescales (Lau and Chan 1988; Madden and Julian 1994). Variability on synoptic–intraseasonal timescales is essentially unpredictable on seasonal–interannual timescales. Therefore, we can essentially view the synoptic–intraseasonal variability as noise on top of the seasonal–interannual variability. We are interested in the potential impact that this noise may have on the low-frequency variability associated with ENSO. Using what is now commonly referred to as generalized linear stability theory, we have examined the spatial structure that a noise forcing field that is stochastic in time must have in order to act as an efficient means of inducing variability on ENSO timescales in the tropical coupled ocean–atmosphere system. This is done using an intermediate coupled ocean–atmosphere model of the tropical Pacific and global atmosphere. It is this aspect of our research that sets it apart from previous studies that have mainly concentrated on the temporal nature of the noise forcing on ENSO. Our results strongly suggest an intimate relationship between intraseasonal variability, such as the Madden–Julian oscillation (MJO), westerly wind burst activity, and ENSO, an idea that agrees with observations of some ENSO episodes, including the 1997/98 event. Based on this result, we concur with those authors cited above that ENSO behaves as a stochastically forced phenomena that has important implications for ENSO prediction and predictability.

The paper is laid out as follows. In section 2 we briefly present some ideas that stem from generalized linear stability theory. The intermediate coupled model used in this study is described in section 3. The response of the coupled model to an imposed stochastic forcing is examined in sections 4 and 5, and the dynamics of the model response is explained in section 6. In section 7 we build on a paradigm of ENSO originally suggested by Lau and Chan (1986, 1988) and we present a discussion of these ideas.

2. Linear theory of a stochastically forced system

We denote by $\mathbf{\Psi}$ the state vector of the seasonal–interannual component of the coupled ocean–atmosphere system at any point in space and time, and assume that the nonlinear development of $\mathbf{\Psi}$ is governed by

$$\frac{\partial \mathbf{\Psi}}{\partial t} = L(\mathbf{\Psi}), \tag{1}$$

where L is a nonlinear operator. As described above, the component of variability on synoptic–intraseasonal timescales can be considered as a stochastic noise-forcing vector $\mathbf{f}(t)$ acting on the system that induces perturbations ψ in the seasonal–interannual component of the system. In sequel, we refer to $\mathbf{f}(t)$ as the ''stochastic forcing'' that varies spatially and temporally, and ψ as the ''coupled system response.'' During their early stages of linear development, when $\psi^2 \ll \psi$, the noise-induced perturbations will be described to first order by

$$\frac{\partial \psi}{\partial t} = \left(\frac{\partial L}{\partial \mathbf{\Psi}}\right)\psi + \mathbf{f}(t). \tag{2}$$

In general $(\partial L/\partial \mathbf{\Psi})$ is nonautonomous and represents a continuous linearization of the system about a time-evolving basic-state solution $\mathbf{\Psi}(t)$ of (1).

For convenience we consider a discrete form of (2) since typically (1) and (2) are solved numerically. Using discrete forms of these equations also greatly simplifies the ensuing algebraic equations making their interpretation more transparent. An appropriate discrete form of the stochastic differential Eq. (2) can be written as

$$\psi_n = \psi_{n-1} + \Delta t \mathbf{A}_{n-1}\psi_{n-1} + (\Delta t)^{1/2}\mathbf{f}_n, \tag{3}$$

where Δt is the time step, and the subscript n refers to the time level $t = n\Delta t$. The matrix $\mathbf{A}_n \equiv (\partial L/\partial \mathbf{\Psi})_{t=n\Delta t}$, and the noise is given by the vector $\mathbf{f}_n \equiv \mathbf{f}(n\Delta t)$. In (3)

we have used a simple time-stepping scheme to simplify the algebraic expressions that follow, but without loss of generality. We will assume that the stochastic forcing is unbiased so that $\langle \mathbf{f}_k \rangle = 0$ and $\langle \mathbf{f}_k, \mathbf{f}_l^T \rangle = D_{k,l}\mathbf{C}$, where $\langle \ldots, \ldots \rangle$ denotes an ensemble average over many different realizations of the noise, $\mathbf{C}$ is the spatial covariance matrix of the noise forcing, $D_{k,l}$ is the temporal decorrelation time of the noise, and the superscript T denotes a matrix transpose. The factor $(\Delta t)^{1/2}$ in the last term of (3) is required to satisfy the variance properties of noise described by a Wiener process (Kloeden and Platen 1992; Penland 1996). Strictly speaking, the discrete form of the stochastic differential Eq. (3) is valid only for white noise forcing. However, if the decorrelation time of the noise is short compared to the timescales typically associated with $\mathbf{A}$ then (3) is still a good approximation (Penland 1996). Kleeman and Moore (1997) have estimated the decorrelation time of real atmospheric noise to be ~3.5 days which is much less than the seasonal–interannual timescales of $\mathbf{A}$. Therefore we expect (3) to be a good discrete approximation to (2).

Of particular interest is the variance of the coupled system response ψ due to the stochastic forcing according to (2). We denote by $\|\psi_n\|_{\mathbf{X}}^2$ the variance of ψ at time $t = n\Delta t$, given by $\|\psi_n\|_{\mathbf{X}}^2 = \langle (\psi_n - \overline{\psi})^T \mathbf{X} (\psi_n - \overline{\psi}) \rangle$, where $\overline{\psi} = \langle \psi \rangle$, and $\mathbf{X}$ defines an appropriate variance-norm. Using (3) the variance can be written as

$$\|\psi_n\|_{\mathbf{X}}^2 = \Delta t \mathrm{Tr}\left\{ \sum_{k=0}^{n-1} \sum_{l=0}^{n-1} D_{l,k} \mathbf{R}_{n,l}^T \mathbf{X} \mathbf{R}_{k,n} \mathbf{C} \right\} \tag{4}$$

(Kleeman and Moore 1997; Farrell and Ioannou 1996a,b), where $\mathbf{R}$ is the propagator of (2) in the absence of the noise $\mathbf{f}$ and is defined by

$$\psi_n = \left\{ \prod_{m=k+1}^{n} (1 + \Delta t \mathbf{A}_{n-m+1}) \right\} \psi_k = \mathbf{R}_{k,n} \psi_k. \tag{5}$$

Therefore in the absence of noise forcing ($\mathbf{f}_n = 0$), $\mathbf{R}_{k,n}$ is the linear operator that advances solutions of (3) forward in time over the time interval $t = k\Delta t \rightarrow n\Delta t$.

It is instructive to rewrite (4) in the following form:

$$\|\psi_n\|_{\mathbf{X}}^2 = \mathrm{Tr}\{\mathbf{ZC}\}, \tag{6}$$

where

$$\mathbf{Z} = \Delta t \sum_{k=0}^{n-1} \sum_{l=0}^{n-1} D_{l,k} \mathbf{R}_{n,l}^T \mathbf{X} \mathbf{R}_{k,n}. \tag{7}$$

If $\mathbf{Z}$ and $\mathbf{C}$ have the eigenvalue/eigenvector sets $\{s_i, \mathbf{S}_i\}$ and $\{p_j, \mathbf{P}_j\}$, respectively, where s_1 and p_1 are the largest eigenvalues, then (6) can be written as

$$\|\psi_n\|_{\mathbf{X}}^2 = \sum_i \sum_j s_i p_j (\mathbf{S}_i \cdot \mathbf{P}_j)^2. \tag{8}$$

The eigenvectors $\mathbf{P}_j$ of $\mathbf{C}$ are the so-called empirical orthogonal functions (EOFs) of the stochastic forcing of the system, and the dominant EOFs represent the spatial patterns that characterize the spatial variability of the noise forcing. The eigenvectors $\mathbf{S}_i$ of $\mathbf{Z}$ are called the ''stochastic optimals'' (Kleeman and Moore 1997; Farrell and Ioannou 1996a,b) and depend on the low-frequency dynamics of the coupled system according to the definition of $\mathbf{Z}$ in (7). The stochastic optimals with the largest eigenvalues are the stochastic forcing field patterns that account for the largest fraction of noise-induced variability. We can think of the spatial structures of the stochastic optimals as the patterns of forcing required to maximize the variability of the coupled system response $\|\psi_n\|_{\mathbf{X}}^2$. Therefore (8) shows that $\|\psi_n\|_{\mathbf{X}}^2$ is determined by the projection of the noise EOFs on the stochastic optimals. The larger this projection, the greater $\|\psi_n\|_{\mathbf{X}}^2$ will be.

Shear flows and asymmetries in the coupled ocean–atmosphere system render the propagator $\mathbf{R}$ non-normal (i.e., $\mathbf{R}^T\mathbf{R} \neq \mathbf{R}\mathbf{R}^T$) (Moore and Kleeman 1999), in which case the eigenvectors of $\mathbf{R}$ and $\mathbf{Z}$ form nonorthogonal sets. The stochastic forcing induces variability $\|\psi_n\|_{\mathbf{X}}^2$ by exciting of the eigenvectors of $\mathbf{R}$ (Farrell and Ioannou 1996a,b). Because these eigenvectors are nonorthogonal, they have a nonzero projection on one another so superpositions of them are characterized by rapid transient growth, even if all of the eigenvectors of $\mathbf{R}$ are stable (Farrell 1985). Therefore in systems where perturbations are described by non-normal dynamics, $\|\psi_n\|_{\mathbf{X}}^2$ can be amplified by stochastic noise forcing. For systems that are unstable in the sense that at least one of the eigenvectors of $\mathbf{R}$ grows in time, the spatial structure of the noise EOFs is less important since any stochastic forcing that perturbs the system will excite the unstable eigenvectors and give rise to variability $\|\psi_n\|_{\mathbf{X}}^2$. However, for systems that are stable, or close to a bifurcation point, the influence of stochastic noise on the low-frequency variability can be extremely important to the behavior of the system as we will demonstrate.

3. Application of linear stability theory to a coupled model

We have applied the ideas of section 2 to the intermediate coupled model of Kleeman (1993) to understand the relationship between intraseasonal variability and interannual variability in the tropical Pacific. This model is currently used operationally for seasonal prediction at the Australian Bureau of Meteorology, and exhibits a relatively high level of predictive skill (Kleeman 1994; Kleeman et al. 1995). It is an anomaly model, and computes anomalous atmospheric and oceanic circulations relative to the mean seasonal cycle of the system that is specified using the observed climatology. Only a brief description of the coupled model is given here, and a detailed account of the model can be found in Kleeman (1993).

a. The atmospheric model

The atmospheric component of the coupled model is a global, linear, Gill-type model described by

$$\epsilon_a U - \beta y V = -\Phi_x$$
$$\epsilon_a V + \beta y U = -\Phi_y$$
$$\epsilon_a \Phi + c_a^2 (U_x + V_y) = -RQ/2, \tag{9}$$

where (U, V) are the anomalous zonal and meridional components of the wind field, Φ is the geopotential height anomaly, $c_a = 60$ m s^{-1} is the equatorial Kelvin wave speed, and $\epsilon_a = (3 \text{ day})^{-1}$ is the coefficient of Rayleigh friction and Newtonian cooling (Kleeman 1989, 1991). The horizontal resolution is 2.8°. The mid-tropospheric heating anomaly Q includes the effects of latent heating due to evaporation and anomalous deep penetrative convection, and is given by

$$Q = \frac{L_v \rho_4 c_E}{c_p \rho_2 I_1} \{ |\mathbf{U}| [q_{\text{diff}}(\overline{T} + T)] + |\overline{\mathbf{U}}| [q_{\text{diff}}(\overline{T} + T) - q_{\text{diff}}(\overline{T})] \} + \frac{L_v I_2}{c_p \rho_2 I_1} [(\overline{q} + q) \nabla \cdot \mathbf{U} + q \nabla \cdot \overline{\mathbf{U}} + (\overline{\mathbf{U}} + \mathbf{U}) \cdot \nabla q + \mathbf{U} \cdot \nabla \overline{q}] + \epsilon_a T. \tag{10}$$

This expression results from integrating the atmospheric moisture equation vertically, where I_1 and I_2 are constants of integration. In (10), L_v is the latent heat of evaporation, c_E is the latent heat exchange coefficient, c_p is the the specific heat capacity at constant pressure, and ρ_4/ρ_2 is the ratio of the air density at 1000 mb to that at 500 mb. An overbar denotes the observed mean value, while all other quantities represent anomalies. In (10), $\overline{T}$ and T are the mean and anomalous sea surface temperature (SST), respectively; $\mathbf{U}$ is the wind velocity; q_{diff} (T) is the air–sea specific humidity difference at temperature T; q is the specific humidity; and $\overline{q}$ the specific humidity at temperature $\overline{T}$. All other symbols have their usual meanings. The term in { . . . } is due to evaporation anomalies while the term in [. . .] represents the effects of anomalous moisture convergence. Penetrative convection in the atmosphere occurs predominantly in areas where SST $>$ 28°C (Graham and Barnett 1987). Circulation anomalies can cause SST to fall below this critical value thus causing penetrative convection to switch off, giving rise to heating anomalies $Q = -\overline{Q}$, where $\overline{Q}$ is the mean latent heating rate computed from observations. This effect is incorporated in the atmospheric model by comparing the moist static energy of air parcels $m(\overline{T} + T)$ with a critical value m_c, below which penetrative convection cannot occur. A full discussion of the form of Q and the condition for penetrative convection is given in Kleeman (1991). The observed seasonal cycle of the coupled ocean–atmosphere system is prescribed in the model through $\overline{T}$, $\overline{\mathbf{U}}$, and $\overline{q}$ in the heating function Q of (10).

The direct thermal forcing term, $\epsilon_a T$, in (10) relaxes the 750-mb geopotential height anomaly to the surface temperature anomaly, a formulation that has been widely used in the literature to mimic the effects of surface processes associated with radiation, sensible heat fluxes, and shallow convection that are not explicitly modelled (e.g., Gill 1985; Davey and Gill 1987). Kleeman (1991) has shown that the effect of this term is very similar to the inclusion of a directly thermally forced boundary layer with realistic stratification.

The performance of the atmospheric model has been the subject of rigorous examination by Kleeman (1991) and Kleeman et al. (1992), and, in general, the model gives a good depiction of the wind anomalies associated with ENSO SST anomalies.

b. The ocean model

The ocean component of the coupled model is limited to the tropical Pacific (30°S–30°N, 115°E and 80°W), with a grid spacing ~½°, and the circulation is described by

$$u_t - \beta y v + g' h_x = \tau_x/\rho_w H_o - \epsilon_o u$$
$$\beta y u + g' h_y = \tau_y/\rho_w H_o \tag{11}$$

and

$$g' h_t + c_o^2 (u_x + v_y) = -\epsilon_o g' h$$
$$T_t - \eta h = -\epsilon T + \kappa T_{xx}, \tag{12}$$

where the equatorial long wave approximation has been made. In (11), (u, v) are the anomalous zonal and meridional surface currents, h is the thermocline depth anomaly, $c_o = 2.3$ m s^{-1} is the equatorial ocean Kelvin wave speed, and $\epsilon_o = (2.5 \text{ yr})^{-1}$ is the oceanic Rayleigh friction and Newtonian cooling coefficient. The equatorial SST anomaly T depends only on the thermocline depth anomaly h,[1] and the parameter η is the constant of proportionality (or regression coefficient) that relates SST anomalies to thermocline depth anomalies h. Different values are used for η in the west and east Pacific to reflect the fact that the main thermocline is deeper in the west than the east. As a result, a given latent heating anomaly is associated with larger SST anomalies in the east than in the west. In the east Pacific from the coast of Central America to 140°W, $\eta = \eta_E = 3.4 \times 10^{-8}$ °C m^{-1} s^{-1}, while in the west Pacific, $\eta = \eta_W = \eta_E/5$. In the central Pacific between 140°W and the

[1] While changes in the rate of vertical and horizontal advection are also known to influence SST (Picaut et al. 1996), Kleeman (1993) has demonstrated that including only the influence of thermocline displacements on SST produces the most skillful coupled model forecasts. This is partly because the thermocline depth variations are described better by the model than are the ocean currents.

date line, η varies linearly between η_E and η_W. Steady-state solutions of (12) yield $T = 2°C$ when $h = 15$ m. The η can also vary seasonally in accordance with the seasonal cycle in mean upwelling. In (12), $|h| \leq h_{\max}$ where $h_{\max}$ is a cutoff value of h that crudely mimics nonlinearities in the real ocean and prevents a runaway instability developing in the coupled system.

Dissipation is present in the model in the form of a negative feedback term (Battisti and Hirst 1989; Neelin 1990), and a weak eddy diffusivity. A fixed Gaussian structure function is used in the meridional direction to compute off equatorial SST anomalies. The *e*-folding length scale of the meridional structure function is 10°, which is close to the atmospheric equatorial radius of deformation. Such a simplification was also made by Neelin (1991) and reflects the assumption that effects such meridional advection and the differing meridional structure of the horizontal modes are unimportant to the primary ENSO mechanism.

The surface wind anomalies computed by the atmospheric model are converted to surface wind stress anomalies τ using the following linear stress law $(\tau_x, \tau_y) = \rho_a c_D \alpha(U, V)$, where ρ_a is the density of air; $c_D = 1.8 \times 10^{-3}$ is a drag coefficient; and $\alpha = 6.5$ m s^{-1} is a representative value of the mean wind speed, which also acts as a coupling coefficient.

The coupled model described here has a number of features in common with the intermediate model of Zebiak and Cane (1987), although the treatment and details of the atmospheric heating differ considerably in the two models.

c. The stochastic noise forcing

By virtue of its intrinsic dynamics the coupled model only describes variability on seasonal–interannual timescales, and in sequel we describe the coupled model symbolically by (1). The ''slaved'' nature of the atmospheric component of the coupled model and the inadequate representation of some of the physical processes that are important for generating synoptic features inhibits the development of variability with timescales shorter than ~1 month, so the coupled model cannot generate a realistic level of internal stochastic noise. Lau and Shen (1988) and Hirst and Lau (1990) discuss this aspect of such models. We will examine the coupled model response to a stochastic noise forcing field, $\mathbf{f}(t)$, that we impose. The advantage of this approach is that we are at liberty to choose different forms for $\mathbf{f}(t)$, and conduct a thorough investigation using a well-understood and computationally inexpensive coupled model.

The response of the coupled system to stochastic forcing can be conveniently analyzed by examining the structure of the stochastic optimals of the coupled model. Recall that the stochastic optimals are the eigenvectors of the operator $\mathbf{Z}$ defined by (7), which depends on the linear propagator $\mathbf{R}$. The propagator for the coupled model was obtained by constructing the first-order linearization of the nonlinear coupled model about the observed seasonal cycle. The transpose propagator $\mathbf{R}^{\mathrm{T}}$ in (7) was computed using the adjoint of the linearized coupled model. Details of the linearized and adjoint coupled models can be found in Moore and Kleeman (1996).

In the following, $\mathbf{X}$ in (7) was chosen so that the (NINO3 index)[2] is the measure of the variability of the coupled system response $\|\psi_n\|^2_{\mathbf{X}}$ defined by (4) where a time interval of $(n - 1)\Delta t = 6$ months was used. The stochastic optimal structures are insensitive to the time interval for $(n - 1)\Delta t \geq 6$ months. Detailed analyses (not shown) reveal that the structure of the stochastic optimals is also insensitive to the choice of $\mathbf{X}$ for time intervals ≥6 months. We will discuss the reason for this in section 6a. Based on the findings of Kleeman and Moore (1997), a decorrelation time of 3.5 days was assumed for $D_{l,k}$, in (4) that agrees with estimates of the real atmospheric noise. However, the results we present are insensitive to this choice of $D_{l,k}$, and a white noise forcing works equally well.

Figure 1a shows the surface heat flux associated with the first stochastic optimal $\mathbf{S}_1$ of the coupled model, the eigenvector of $\mathbf{Z}$ with the largest eigenvalue.[2] The dominant feature of the stochastic optimal heat flux is the dipole centered on the western tropical Pacific. The wind stress component of the stochastic optimal $\mathbf{S}_1$ is shown in Fig. 1b and takes the form of bands of predominantly zonal winds. Based on the discussion of (8), Fig. 1 represents the preferred pattern of stochastic forcing that the coupled model would like to ''feel'' in order to increase its variability $\|\psi_n\|^2_{\mathbf{X}}$, so if the spatial structure of the EOFs of the noise forcing resemble $\mathbf{S}_1$ of Fig. 1, then according to (8) the stochastic forcing will increase $\|\psi_n\|^2_{\mathbf{X}}$. The physical factors responsible for the structure of the stochastic optimal are complex and have been examined by Moore and Kleeman (1999).

The structure of the stochastic optimal in Fig. 1 obviously depends on the intrinsic dynamics of the coupled model. However, given the high level of predictive skill exhibited by the coupled model (Kleeman 1993) we believe that the model describes dynamics that are important for ENSO variability. Analyses by Kleeman and Moore (1997) show that the wind pattern in Fig. 1b accounts for a large fraction of the real atmospheric noise as estimated from European Centre for Medium-Range Weather Forecasts (ECMWF) wind data. A similar analysis was not possible for the surface heat flux because of the lack of a long and reliable observational dataset. However, the surface heat flux component of the stochastic optimal resembles observed heat flux

[2] We show only the first stochastic optimal because analyses have shown that this pattern alone accounts for a large fraction of the real atmospheric noise estimated from ECMWF wind data (Kleeman and Moore 1997a).

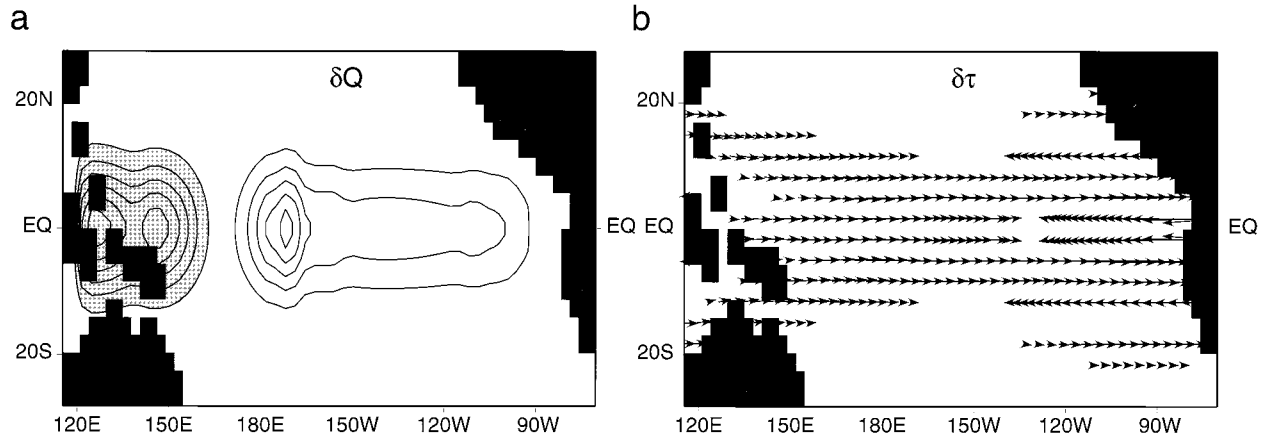

FIG. 1. The first member $\mathbf{S}_1$ of the stochastic optimal spectrum of the coupled model assuming a decorrelation time of 3.5 days for the stochastic noise: (a) the surface heat flux, (b) the surface wind stress. In (a) shaded and unshaded regions are of opposite sign. The contour interval and arrow scaling is arbitrary.

anomalies associated with intraseasonal variability (see the observations of Lau and Chan 1985, 1988; Jones and Weare 1996; Hendon and Glick 1997). Therefore, it is possible that intraseasonal variability, such as the MJO, can act as a source of noise forcing for variability on ENSO timescales, an idea originally proposed by Lau and Chan (1986, 1988). We will now explore this idea further.

4. Stochastically forced solutions of the coupled model

To examine the potential influence of stochastic forcing on the variability of the coupled system, we ran the nonlinear coupled model subject to stochastic noise forcing. Analyses of ECMWF wind products (Kleeman and Moore 1997) indicate that $\mathbf{S}_1$ and $\mathbf{S}_2$ are present in the real atmospheric wind field noise with significant amplitudes, approximately in the ratio 10:1, respectively. The signatures of other members of the stochastic optimal spectrum have insignificant amplitudes. A noise field was constructed so that $\mathbf{f}(t) = a_1(t)\mathbf{S}_1 + a_2(t)\mathbf{S}_2$ and $(\overline{a_1^2})^{1/2} = 10(\overline{a_2^2})^{1/2}$ where an overbar denotes a time average. The amplitudes a_1 and a_2 were generated using an autoregressive model with a decorrelation time of 3.5 days and forced by white noise from a random number generator. At each point the noise forcing has a zero time mean, that is, $\overline{a_1} = \overline{a_2} = 0$. Averaged over the tropical Pacific, the standard deviation σ_T of the noise forcing on SST is 1.2×10^{-2} K day^{-1}, which for a 50-m-deep ocean surface mixed layer corresponds to surface heat flux noise with standard deviation $\sigma_H = 27$ W m^{-2}. Most of this variance occurs west of 155°W where $\sigma_T = 1.4 \times 10^{-2}$ K day^{-1} (equivalent to $\sigma_H = 33$ W m^{-2} for a 50-m ocean mixed layer). These amplitudes are consistent with direct surface flux measurements made during (TOGA the Coupled Ocean–Atmosphere Response Experiment COARE; Hendon and Glick 1997). East of 155°W, $\sigma_T = 8 \times 10^{-3}$ K day^{-1} ($\sigma_H = 18$ W m^{-2}). The standard deviation σ_W of the surface wind speed over the entire tropical Pacific is 0.3 m s^{-1} ($\sigma_W = 0.16$ m s^{-1} west of 155°W, and $\sigma_W = 0.24$ m s^{-1} east of 155°W). The wind-noise amplitude is somewhat lower than observed during TOGA COARE, but as shown in section 6a, the noise forcing quickly initiates rapidly growing coupled ocean–atmosphere perturbations that strongly resemble observed intraseasonal variability. Therefore, part of what might be considered as an observed component of the wind stress noise actually develops in the model through air–sea interactions. This suggests that the observed intraseasonal variability may be governed by coupled air–sea interactions. Evidence from simple models (Lau and Shen 1988; Hirst and Lau 1990), coupled general circulation models (Rosati and Stern 1998, personal communication), and observations (Krishnamurti et al. 1988; Sperber et al. 1997) strongly supports this idea. The sensitivity of the coupled model to stochastic forcing amplitude is examined in section 6e.

The stability of the coupled model depends on various parameters as described in section 5. Parameters given in section 3a and 3b render the coupled model stable to perturbations in the sense that it does not support self-sustaining oscillations.[3] Therefore in the absence of any forcing, all anomaly fields are damped and quickly tend to zero, and there is no variability $\|\psi_n\|_{\mathbf{x}}^2$ in the

[3] We use this definition of stability rather loosely. In the strictest sense, in a truly linearly unstable system perturbations would grow without bound. In the coupled model, the amplitude of the self-sustaining oscillations is growth limited by the nonlinearities described in section 3. Battisti and Hirst (1989) report a similar dependence of oscillation amplitude on nonlinearities in the model of Zebiak and Cane (1987).

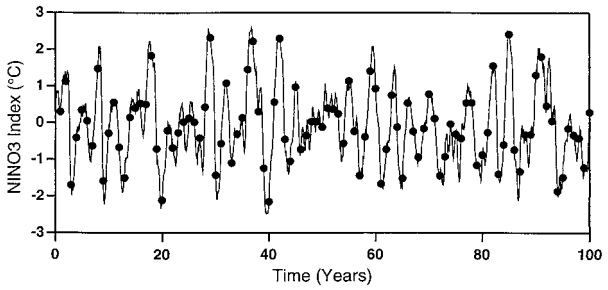

FIG. 2. A time series of the NINO3 index from a 100-yr integration of the coupled model forced with stochastic noise composed of $\mathbf{S}_1$ and $\mathbf{S}_2$. The bullets indicate 1 Dec of each year.

system, so the NINO3 and SOI indices would be zero at all times.

Figure 2 shows a 100-yr time series of the NINO3 index from the nonlinear coupled model forced with the stochastic noise field described above. Despite the relatively low amplitude of the noise forcing, Fig. 2 shows that sizable SST anomalies develop in the NINO3 region, and that noise-induced, aperiodic, variability in the coupled model on seasonal–interannual timescales is remarkably realistic. The ''bullets'' in Fig. 2 indicate 1 December of each year, and there is a tendency for the peak of large amplitude warm and cold episodes to be phase-locked with the seasonal cycle. We discuss this aspect of the model behavior further in section 6. The power spectrum of the model NINO3 index is shown in Fig. 3 where it is compared to the spectrum of the observed NINO3 index. The spectra in Fig. 3 were computed using a maximum entropy method of order 30 (Press et al. 1996) to aid comparison of our results with the recent related works of Blanke et al. (1997) and Eckert and Latif (1997). The observed NINO3 time series is from the period 1875 to 1996, and is described in detail by Torrence and Webster (1998). Figure 3 shows that the shape of the model NINO3 index spectrum agrees fairly well with that of the observations. However the power in the frequency band $>(2\ \text{yr})^{-1}$ is higher than observed, a feature that can be partly corrected by reducing the stochastic forcing amplitude (see section 6e).

Figure 2 clearly shows that there are decadal variations in the noise-induced ENSO variability of the coupled model. We ran the stochastically forced integration of Fig. 2 for an additional 900 yr to obtain statistically significant signals over a wide range of frequencies, and Fig. 4a shows a wavelet power spectrum of the model NINO3 index as a function of period using a Morlet wavelet (Meyers et al. 1993). Recall that the stochastic noise forcing has a decorrelation time of 3.5 days. Figure 3 however shows that the coupled model response is ''red.'' The statistical significance of the wavelet spectra were therefore computed by comparison with a mean background red-noise spectrum. If a peak in the wavelet power spectrum is significantly above this background then a confidence level is assigned to the peak using a

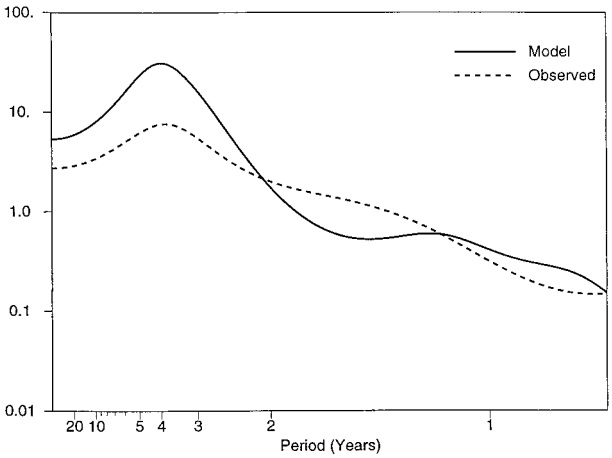

FIG. 3. A comparison of the power spectrum of the NINO3 index from the stochastically forced coupled model and observation. The spectra were computed using a maximum entropy method of order 30.

chi-squared test as described by Torrence and Compo (1998). Most of the variability occurs in the 3–8-yr period band, and is associated with model ENSO episodes. Variability in the 3–8-yr band is episodic being pronounced during some time intervals and absent during others as illustrated in Fig. 4b that shows an expanded view of the wavelet time series between years 100 and 200. To demonstrate that this kind of variability is not a manifestation of the noise forcing spectrum, Fig. 4c shows a wavelet analysis of the 1000-yr noise forcing amplitude time series that was used where the same red-noise model is used to test for statistical significance. If we denote the wavelet power spectrum of the model NINO3 index as $S_T(\omega, t)$ where ω is frequency and t is time, and the corresponding wavelet spectrum of the noise forcing amplitudes as $S_N(\omega, t)$, then a measure of the degree of correspondence between Figs. 4a and 4c is the correlation

$$r(\omega) = \frac{\overline{[S_T(\omega, t) - \overline{S_T(\omega)}][S_N(\omega, t) - \overline{S_N(\omega)}]}}{\{\overline{[S_T(\omega, t) - \overline{S_T(\omega)}]^2}\ \overline{[S_N(\omega, t) - \overline{S_N(\omega)}]^2}\}^{1/2}}, \tag{13}$$

where an overbar indicates an average over time, and $\overline{S_T(\omega)}$ and $\overline{S_N(\omega)}$ are the time-mean values of S_T and S_N, respectively. Values of $r(\omega)$ are also shown in Fig. 4c for each frequency band. Clearly there is no significant correlation at any frequency between the NINO3 index spectrum of Fig. 4a and the noise spectrum of Fig. 4c.

The decadal variations of ENSO activity in Fig. 4b are very reminiscent of the kinds of observed decadal variations in the NINO3 index. Figure 4d from Torrence and Compo (1998) shows a wavelet analysis of the observed NINO3 index from 1875 to the present. Changes in ENSO activity and changes in the frequency band of maximum power are reminiscent of the kinds of changes occurring in the stochastically forced model. Therefore,

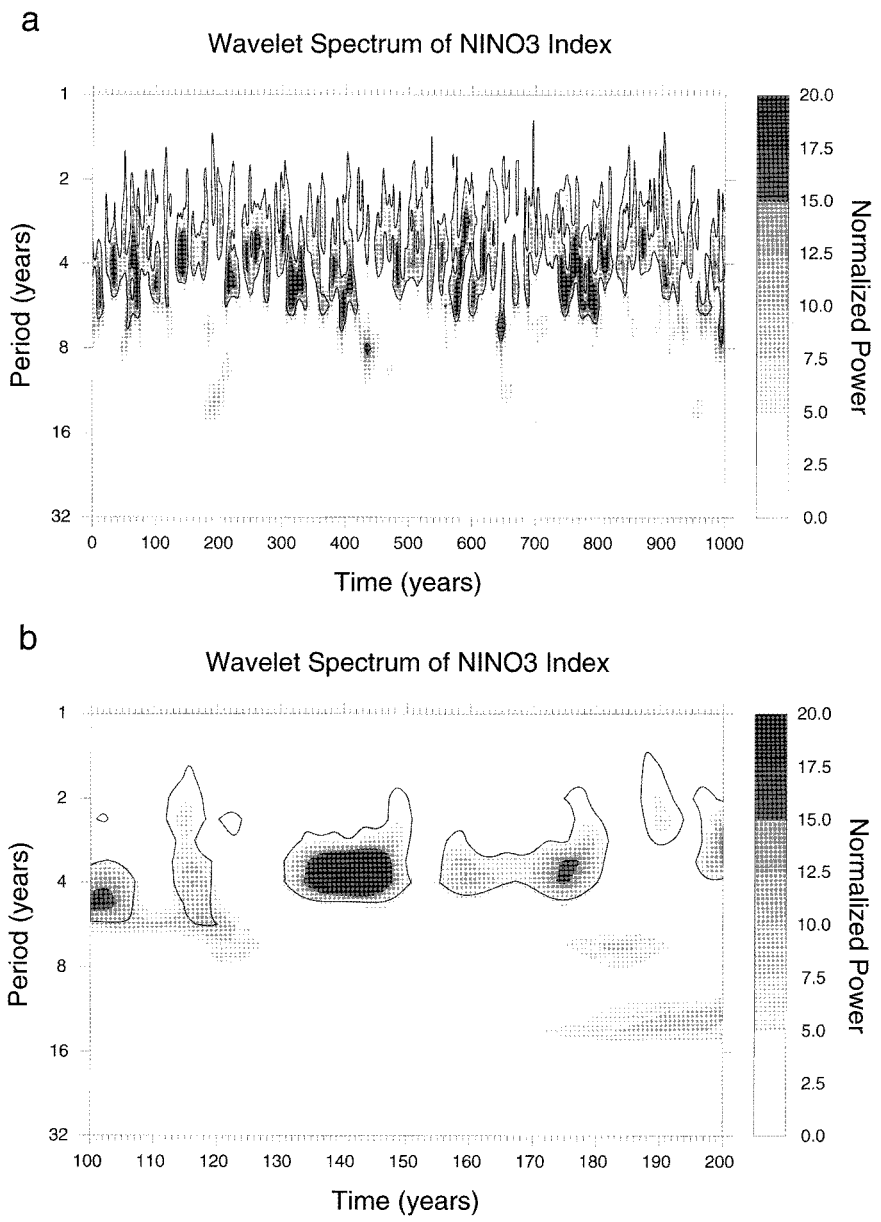

FIG. 4. (a) A wavelet power spectrum of the NINO3 index time series from a 1000-yr integration of the coupled model forced with stochastic noise. (b) As in (a) but showing the details of the wavelet spectrum between years 100 and 200. (c) A wavelet power spectrum of the 1000-yr stochastic forcing time series. Also shown is the correlation $r(\omega)$ defined in the main text for each periodic time indicated on the left of the wavelet spectrum. Note the difference in the scale between (a) and (c). (d) A wavelet power spectrum of the observed NINO3 index from Torrence and Compo (1998). The shaded contours are normalized variances of 1, 2, 5, and 10. Cross-hatching regions indicate the ''cone of influence'' where edge effects due to the finite length of the time series become important. In each panel the bold contour represents the 95% confidence level for a red-noise process.

it is reasonable to believe that stochastic forcing of the coupled system due to variations in atmospheric and oceanic transient activity may be a possible cause of the changes on decadal timescales that are seen in the observations, an idea discussed further in section 7.

To demonstrate the importance of the spatial structure of the noise forcing for inducing low-frequency variability in the coupled model, Fig. 5 shows a 100-yr time series of NINO3 index when the noise forcing is white in space with a 3.5-day decorrelation time, and has the same amplitude as before. In this case the coupled system response has a very low amplitude.

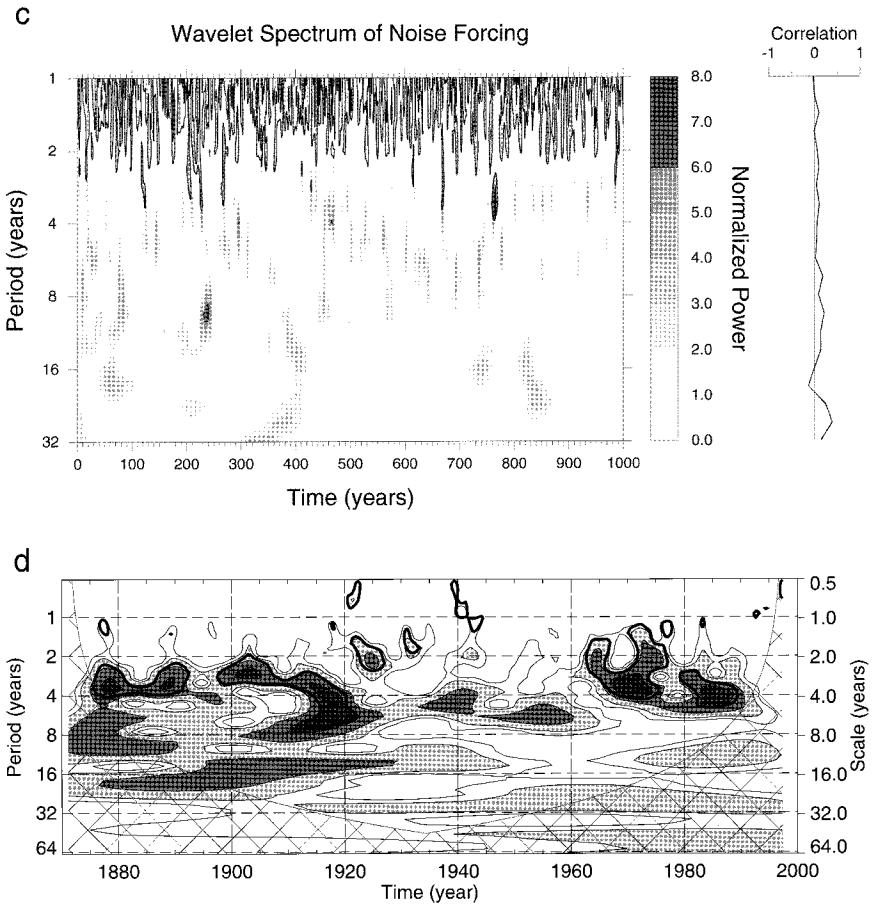

FIG. 4. (*Continued*)

5. Variations in the stability of the coupled system

The stability of the coupled model affects the character of the ENSO oscillations that it can support, and depends upon a number of important parameters related to the large-scale circulations of both the ocean and atmosphere. Damped or self-sustaining oscillations are solutions of the model depending on the parameters chosen, and the coupled system response to stochastic forcing is sensitive to the character of the ENSO oscillations the system can support.

Three important parameters (described in section 3) that strongly influence the behavior of the coupled model are

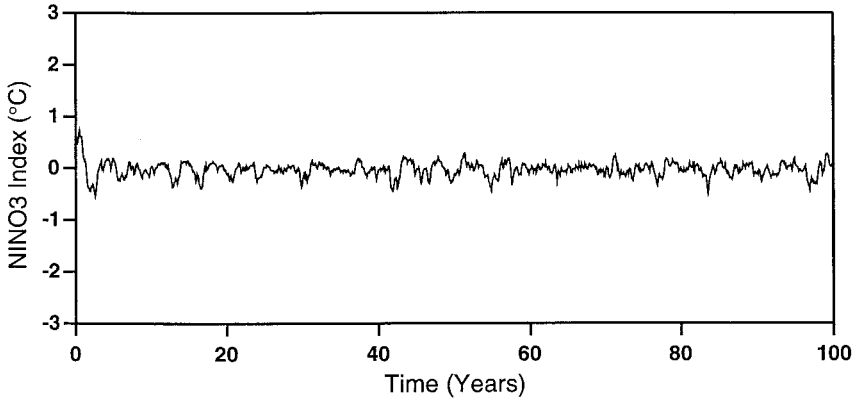

FIG. 5. A time series of the NINO3 index from a 100-yr integration of the coupled model forced with stochastic noise that is white in space with a 3.5 day decorrelation time.

1) the ocean–atmosphere coupling strength, α.;
2) the phase speed, c_0, of the equatorial ocean Kelvin wave; and
3) the sensitivity, γ, of the SST anomalies to vertical movements in the main ocean thermocline. This is incorporated in (12) by replacing ηh by $\gamma\eta h$. As defined, γ is a dimensionless number, where $\gamma = 1$ corresponds to the default sensitivity used in Fig. 2, and $\gamma = a$ represents the case where SST is a times more sensitive to thermocline movements than the default case.

The stochastically forced coupled model run described in section 4 was repeated using all possible combinations of α, c_0, and γ for $\alpha = 4.0$, 6.5, 9.0 m s^{-1}, $c_0 = 1.6$, 2.3, 3.0 m s^{-1}, and $\gamma = 0.5$, 1.0, 1.5. These modest parameter ranges certainly lie within the realms of the real coupled system. The central values $\alpha = 6.5$ m s^{-1}, $c_0 = 2.3$ m s^{-1}, $\gamma = 1.0$ are identical to the case shown in Fig. 2, and a normal mode analysis of the system reveals that the model is stable and very close to its bifurcation point (see Moore and Kleeman 1997b).

Figure 6 shows 100-yr time series of NINO3 index for the stochastically forced nonlinear coupled model for each of the 27 different combinations of the parameters α, c_0, and γ. Clearly the stochastically forced coupled system response varies considerably from case to case. In Fig. 6, the parameter combinations for which the coupled model will not support self-sustaining oscillations are denoted ''S'' for stable, those which do support self-sustaining oscillations are denoted ''U'' for unstable, and those cases that are stable but close to the primary bifurcation point of the model are denoted ''B.'' Stable systems far from the primary bifurcation point (such as $\gamma = 0.5$ for all α and c_0) produce low amplitude, essentially stochastic responses in the NINO3 region in response to the noise forcing. As anticipated, unstable systems (such as $\alpha = 9$ m s^{-1}, $\gamma = 1$, for all c_0) produce regular, self-sustaining oscillations. The unstable cases become more irregular as the amplitude of the stochastic forcing is increased substantially (see section 6e). Most interesting are the stable cases close to the primary bifurcation point where the coupled model produces realistic timeseries of variability as discussed in section 4.

The real ocean–atmosphere counterparts of α, c_0, and γ depend on many environmental factors controlled by the atmospheric and oceanic circulations. Slow changes in the large-scale components of these circulations on climatic timescales will also influence α, c_0, and γ, so it is reasonable to suppose that decadal to centennial timescale variations in climate will influence the stablity of the coupled system. Therefore, if stochastic forcing is important for initiating ENSO episodes, the character of the ENSO variability we observe will depend on where the real coupled system resides with respect to its primary bifurcation point. As the real coupled system slowly ''wanders'' through parameter space we might

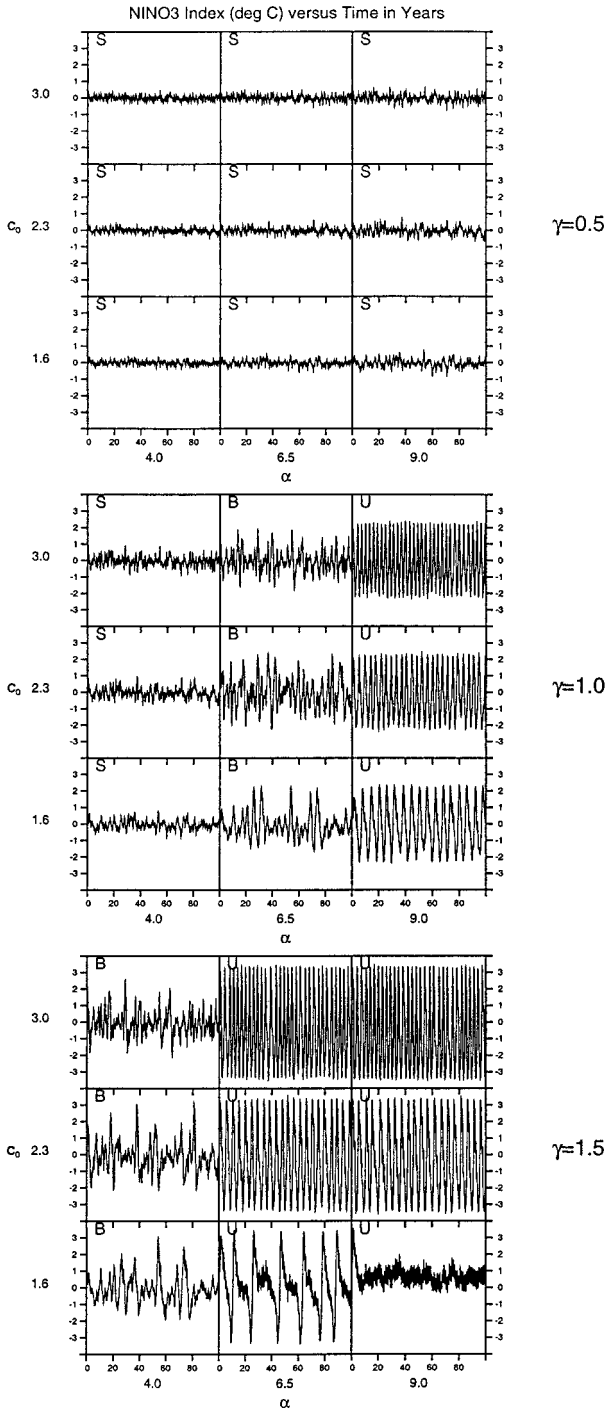

FIG. 6. Time series of the NINO3 index from 100-yr integrations of the coupled model forced with stochastic noise as a function of α, c_0, and γ. The noise forcing is composed of $\mathbf{S}_1$ and $\mathbf{S}_2$. The letters S and U indicate that system is stable or unstable, respectively, while the letter B indicates that the system is stable but close to its primary bifurcation point.

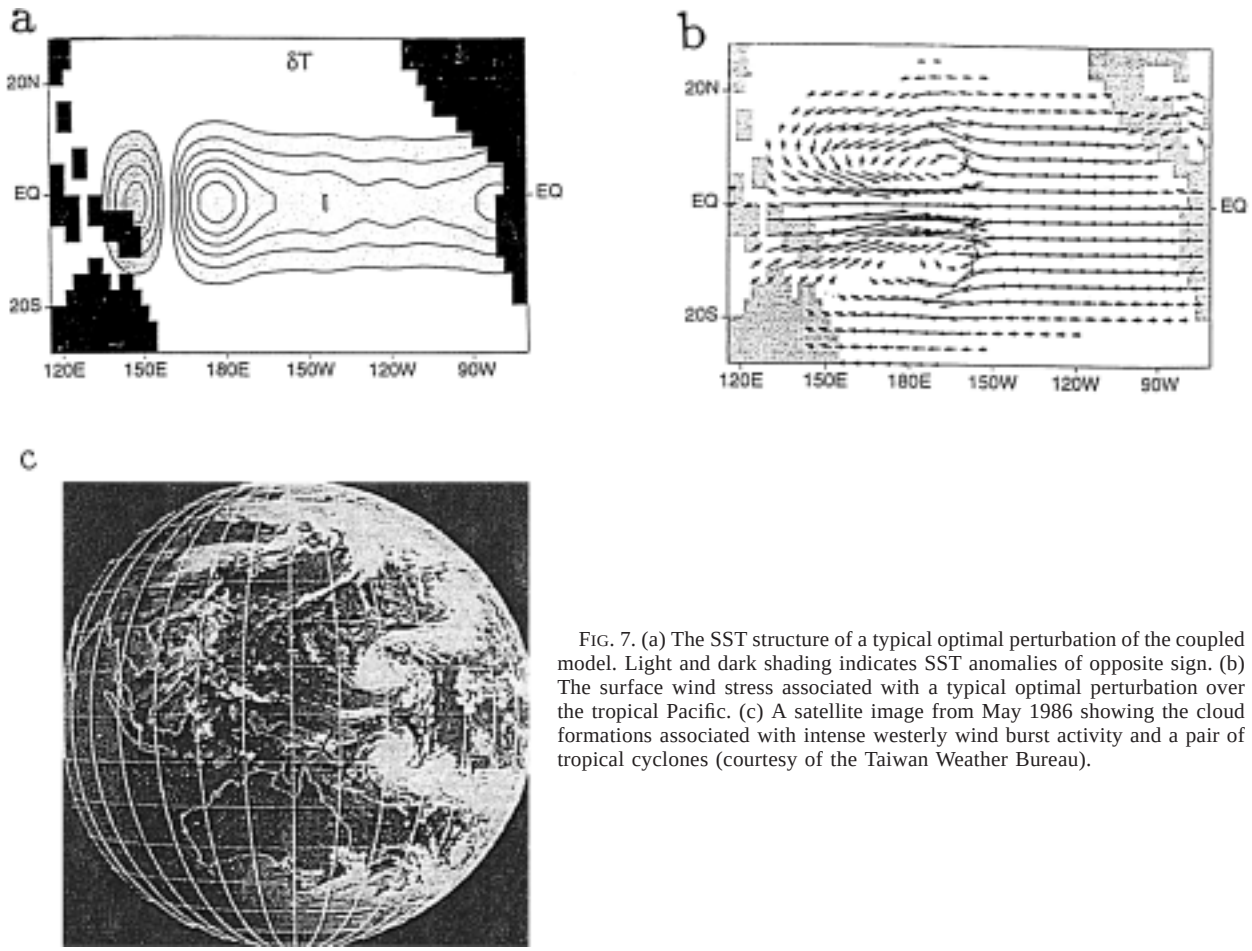

FIG. 7. (a) The SST structure of a typical optimal perturbation of the coupled model. Light and dark shading indicates SST anomalies of opposite sign. (b) The surface wind stress associated with a typical optimal perturbation over the tropical Pacific. (c) A satellite image from May 1986 showing the cloud formations associated with intense westerly wind burst activity and a pair of tropical cyclones (courtesy of the Taiwan Weather Bureau).

therefore expect to see changes in the character of ENSO variability. This is an alternative and complementary explanation to that discussed in section 4 for observed decadal variations in ENSO activity.

6. The dynamics of noise-induced interannual variability

a. Optimal perturbations

1) OPTIMAL PERTURBATION STRUCTURES

Under the influence of stochastic noise forcing, the ENSO variability that develops in the model is maintained by stochastically induced perturbations that resemble ''optimal perturbations.'' The optimal perturbations are the eigenvectors φ of the generalized eigenequation $\mathbf{R}^{\mathrm{T}}\mathbf{X}\mathbf{R}\varphi = \lambda\mathbf{X}\varphi$ with eigenvalues λ (Farrell 1985) and represent the fastest growing perturbations that can exist in the coupled system before nonlinearity becomes important. For the stochastic optimal in Fig. 1, $\mathbf{X}$ defines the (NINO3-Index),[2] so optimal perturbations for this norm produce the fastest growth of (NINO3-Index).[2] These perturbations compose a superposition of the eigenvectors of $\mathbf{R}$ (i.e., the traditional normal modes or finite-time modes of the system). While each individual eigenvector of $\mathbf{R}$ decays in time for the standard parameter choice in Fig. 2, the superposition of eigenvectors that make up the optimal perturbation undergoes rapid transient growth. Figure 7a shows the SST structure of a typical optimal perturbation that bears a strong resemblence to the stochastic optimal surface heat flux of Fig. 1, and resembles some phases of observed SST anomalies associated with the MJO (compare Fig. 7 with Fig. 8 of Hendon and Glick 1997). Therefore, when the coupled system is subjected to stochastic noise forcing that projects on the stochastic optimals, perturbations with initial structures that are similar to the optimal perturbations are excited and subsequently grow rapidly. These perturbations act as efficient precursors for ENSO episodes (Moore and Kleeman 1996), so stochastically induced perturbations can spawn ENSO episodes, thereby increasing the low-frequency variability of the system as required by the linear theory of section 2. These ideas are also supported by the analyses of Penland and Sardeshmukh (1995) and Penland (1996) who computed the optimal perturbations of observed SSTs in the tropical Pacific and Indian Oceans and find that SST anomalies prior to ENSO

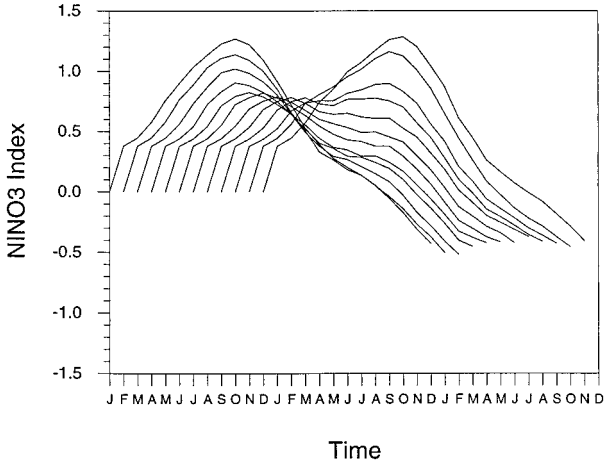

FIG. 8. Two-year time series of NINO3 index from the coupled model subjected to the $-/+$ phase of $\mathbf{S}_1$ with constant amplitude for the first 14 days and zero forcing amplitude thereafter. Each curve corresponds to an integration of the model started on the first of each month.

episodes project heavily on the fastest growing optimal perturbation.

The wind stress pattern of a typical optimal perturbation is shown in Fig. 7b that bears a remarkable resemblence to westerly wind bursts frequently observed in the western tropical Pacific, often in connection with the MJO. Figure 7c shows a satellite image of the cloud formations associated with strong westerly wind bursts and an accompanying tropical cyclone pair that occured during May 1986. The similarity between the optimal perturbation of Fig. 7b and the observations of Fig. 7c is striking. Moore and Kleeman (1997b) have shown that all of the observed characteristics of westerly (and easterly) wind bursts in relation to their duration, longitudinal extent, associated cyclone activity, etc., can be captured by the optimal perturbations of the coupled model. In the model, variations in the phase of the seasonal cycle, as well as the relative importance of different thermodynamic processes in the upper ocean that control SST, account for the changes in the characteristics of the optimal perturbation wind bursts.

Recall that the stochastic optimals depend on the variance-norm defined by $\mathbf{X}$. Experiment shows that the basic structure of the stochastic optimals is insensitive to the choice of $\mathbf{X}$ in (7) for time intervals $(n - 1)\Delta t \geq 6$ months. This is because the kernel in (7) becomes dominated by $\mathbf{R}^{\mathrm{T}}$ as $(n - 1)\Delta t$ increases. For time intervals $\geq$6 months the eigenvectors of $\mathbf{R}^{\mathrm{T}}$ emerge as the adjoint coupled model is integrated backward in time and their structure dominates the eigenvectors of $\mathbf{Z}$. The gravest eigenvector of $\mathbf{R}^{\mathrm{T}}$ is the optimal excitation for the gravest eigenvector of $\mathbf{R}$ (Farrell 1989), where the latter describes ENSO in this model (Moore and Kleeman 1999). Similarly the structure of the optimal perturbations is relatively insensitive to the choice of $\mathbf{X}$ (Moore and Kleeman 1997b) and they have structures similar to the gravest eigenvector of $\mathbf{R}^{\mathrm{T}}$. Hence the stochastic optimal generates perturbations that stongly resemble the optimal excitations for the model ENSO.

To demonstrate the role played by optimal perturbations in enhancing the variability of the coupled system response, the coupled model was run for 2 yr subject to constant amplitude forcing composed of $\mathbf{S}_1$ (cf Fig. 1) during the first 14 days of integration after which time the forcing amplitude was zero. This type of forcing is very reminiscent of an isolated MJO episode. The standard deviation of the noise forcing averaged over the tropical Pacific was $\sigma_H = 40$ W m^{-2} and $\sigma_W = 0.5$ m s^{-1}. The model parameters used are the same as those in Fig. 2. The model was run in this way 12 times starting from the first day of each calender month. In each case the stochastic optimal forcing had a negative heat flux anomaly over the far west Pacific, and a positive anomaly over the central and eastern Pacific. For simplicity, this configuration of the stochastic optimal will be referred to symbollically as "$-/+$." The opposite phase of the stochastic optimal which is the negative of that shown in Fig. 1 will be referred to as "$+/-$."

Figure 8 shows the 2-yr time series of the NINO3 index from model runs started each month. In each case a warm episode initially develops with a SST anomaly $\sim$1°C in the central Pacific in response to the forcing. (Recall that the model is stable in the sense that the NINO3 index is zero at all times in the absence of any forcing.) The amplitude of the SST anomaly is largest for cases forced between September and March when each episode peaks around October–November. This suggests that the episode peak is phase locked with the seasonal cycle similar to observed events (Rasmusson and Carpenter 1982). The dynamical reasons for this phase-locking, also apparent in Fig. 2, will be discussed shortly. When the experiments of Fig. 8 were repeated using the $+/-$ pattern of the stochastic optimal, the model initially developed a cold episode in all cases, phase-locked to the seasonal cycle as in Fig. 8.

2) HEAT FLUX VERSUS WIND STRESS

Since the dynamics of the noise-induced perturbations in Fig. 8 are approximately linear during the first few months, we can explore the relative roles played by the surface heat flux and wind stress components of the $\mathbf{S}_1$ forcing during this period. To do this, the coupled model was started on 1 January, and forced for 14 days as in Fig. 8, but with the $\mathbf{S}_1$ heat flux and wind stress components used separately. After 14 days, the noise forcing was zero. The structure of the thermocline depth, h, and SST fields, T, that result from the surface heat flux forcing alone are shown in Fig. 9 during months 2–4, and are very similar to those of the optimal perturbations of the coupled model examined by Moore and Kleeman (1996). Figure 10 from Moore and Kleeman (1996) shows the evolution of the thermocline perturbation for

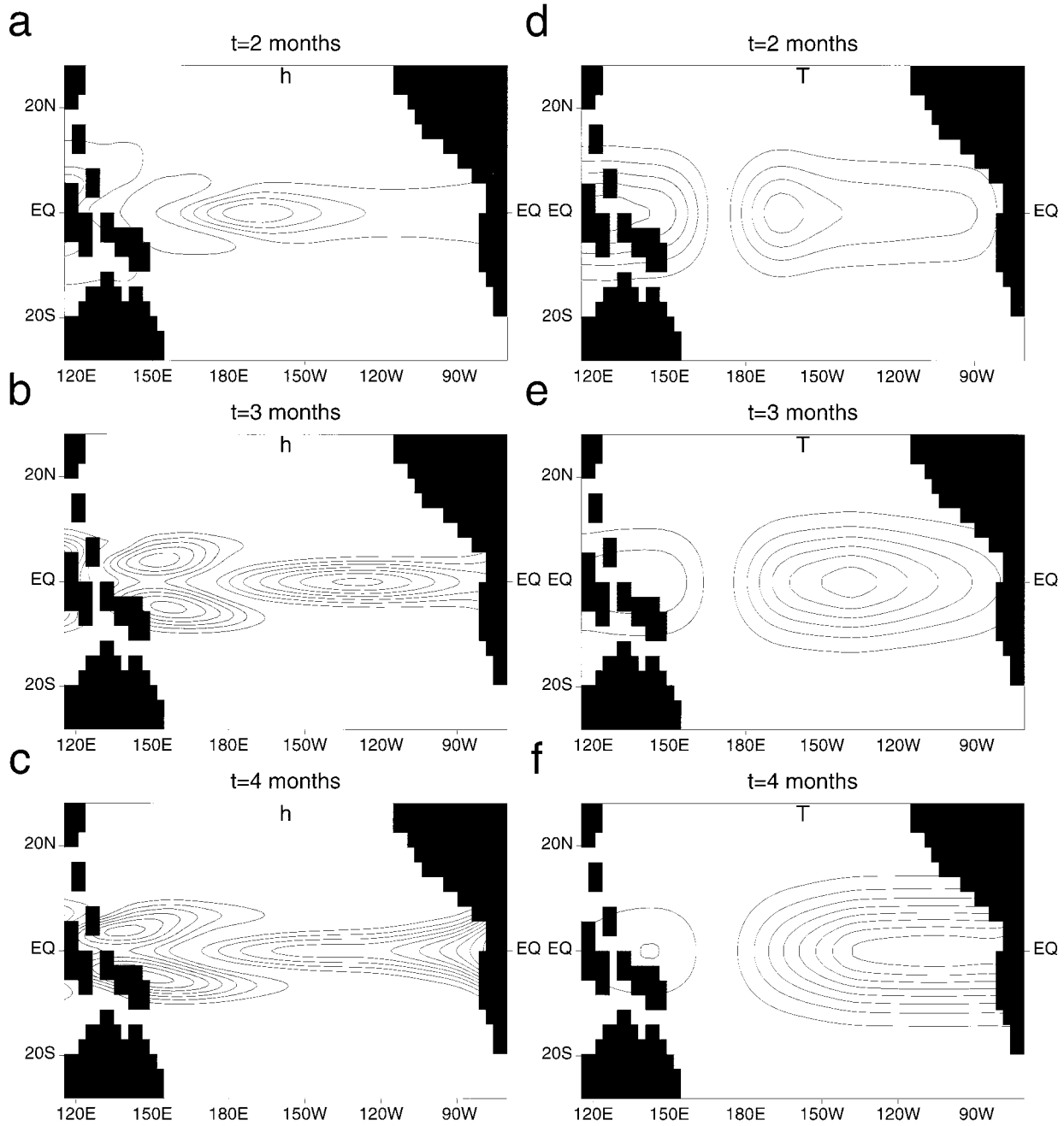

FIG. 9. Contour maps of thermocline depth, *h*, and SST, *T*, for months 2–4 from the coupled model when subjected to the −/+ phase of the surface heat flux component of $\mathbf{S}_1$ with constant amplitude for 14 days starting on 1 Jan. Shaded and unshaded regions are of opposite sign. In (a)–(c) the contour interval is 0.75 m, and in (d)–(f) the contour interval is 0.05°C.

a typical optimal perturbation, which like Figs. 9a–c, takes the form of an eastward propagating Kelvin wave. The dipole structure in the SST of Figs. 9d–f is similar to that shown in Fig. 7a and produces a wind field response (not shown) like that shown in Fig. 7b.

The structures of *h* and *T* that result from the wind component of $\mathbf{S}_1$ alone are shown in Fig. 11. These perturbations also take the form of a Kelvin wave in the *h* field, driven mainly by the zonally banded wind structure of $\mathbf{S}_1$ over the central and eastern Pacific (cf Fig. 1b). Because both the surface heating and wind stress components of $\mathbf{S}_1$ tend to generate perturbations with structures similar to the optimal perturbations, it is not necessary for both components of the noise forcing to be present at the same time. To illustrate, Fig. 12 shows the NINO3 index from the coupled model when

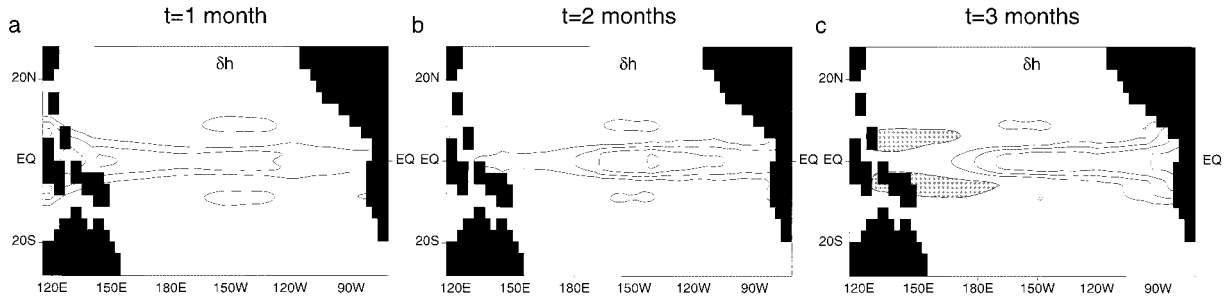

FIG. 10. Contour maps of thermocline depth perturbation, δh, for a typical optimal perturbation of the coupled model. The contour interval is 1.5 m.

forced with (a) the surface heat flux component alone, and (b) the wind stress component alone, of the stochastic optimals. The amplitude of the forcing in this case is $\sigma_H = 54$ W m^{-2} and $\sigma_W = 0.6$ m s^{-1}, which is twice that used in the experiment of Fig. 2. The two components of the noise forcing produce almost identical time series of the NINO3 index, which are also very similar to that of Fig. 2. To understand this, recall that the stochastic optimal of Fig. 1 resembles the gravest eigenvector of $\mathbf{R}^{\mathrm{T}}$, which is the optimal excitation for the model ENSO. The stochastic optimal therefore generates perturbations that project heavily onto the model ENSO, thereby increasing $\|\psi_n\|_X^2$. The model ENSO is an oscillation with an atmospheric and oceanic component, so $\mathbf{S}_1$ must produce atmospheric and oceanic perturbations that produce the same phase of ENSO (i.e., the two components add constructively). The heat flux (wind stress) component of the stochastic optimal excites the atmospheric (oceanic) component of ENSO. Hence, each component of $\mathbf{S}_1$ applied separately with the same temporal structure produces a NINO3 time series in which the ENSO episodes have the same amplitude and phase. Therefore the stochastically induced variability produced by the two components of $\mathbf{S}_1$ is the same, while nonlinear effects account for some of the differences in Fig. 12. The dynamical, reasons for the difference in structure between the stochastic optimal $\mathbf{S}_1$ and the model ENSO are discussed in detail by Moore and Kleeman (1999).

Further experiments (not shown) reveal that it is the surface heat flux component of $\mathbf{S}_1$ in the west Pacific that has the largest impact on the variability of the system, while it is the $\mathbf{S}_1$ wind stress over the eastern Pacific that has most impact on the variability. This can be understood by examining the structure of the gravest eigenvector of $\mathbf{R}^{\mathrm{T}}$, which bears a strong resembence to the stochastic optimal, and is the optimal excitation for the model ENSO. Detailed analyses by Moore and Kleeman (1999) have revealed that the west and east Pacific are the centers of action for SST and the ocean circulation, respectively, for this eigenvector. As noted earler, the stochastic optimal heat flux in the west resembles heating anomalies associated with the MJO and intraseasonal variability. A comparison of Fig. 1b with EOF analyses of Hendon and Glick (1997, see their Fig. 8) reveals that the banded structure of the $\mathbf{S}_1$ wind stress in the eastern Pacific is consistent with changes in the tropical trade winds that occur when a MJO event passes through the system. Some of the stochastic optimal structure in the east may also be representative of synoptic variability in this region, and variability in the intertropical convergence zone.

3) PHASE-LOCKING TO THE SEASONAL CYCLE

The phase-locking of the stochastically induced ENSO episodes in Figs. 2 and 8 can be understood in terms of optimal perturbation dynamics. Moore and Kleeman (1996) have shown that the seasonal cycle of SST (which recall is specified from observations in the model) is a major factor controlling seasonal variations in optimal perturbation growth rates. During the period January–April, the warm pool moves eastward raising the SST in the central Pacific, and creating conditions there that are favorable for rapid perturbation growth through perturbations in deep penetrative convection. Moore and Kleeman (1996, 1997b) show that mean moisture convergence by the perturbation wind is the most important term in the energy budget of the optimal perturbations, a mechanism also identified by Lau and Shen (1988) and Hirst and Lau (1990) as important for the development of coupled ocean–atmosphere modes on intraseasonal timescales. The wind–evaporation feedback suggested by Emmanuel (1987) and Neelin et al. (1987) as a mechansim for rapid perturbation growth in the tropical atmosphere does not play a major role in the model used here. The optimal perturbations of Fig. 7 grow toward the east (Moore and Kleeman 1997a) since their SST is influenced only by thermocline perturbations. Therefore, if a perturbation can grow toward the east and achieve a large amplitude before the warm pool begins to move westward again, then it can have a significant effect on the seasonal–interannual variability. Perturbations that develop late or early in the year have up to 6 months to achieve a large amplitude in this way, and as shown by Moore and Kleeman

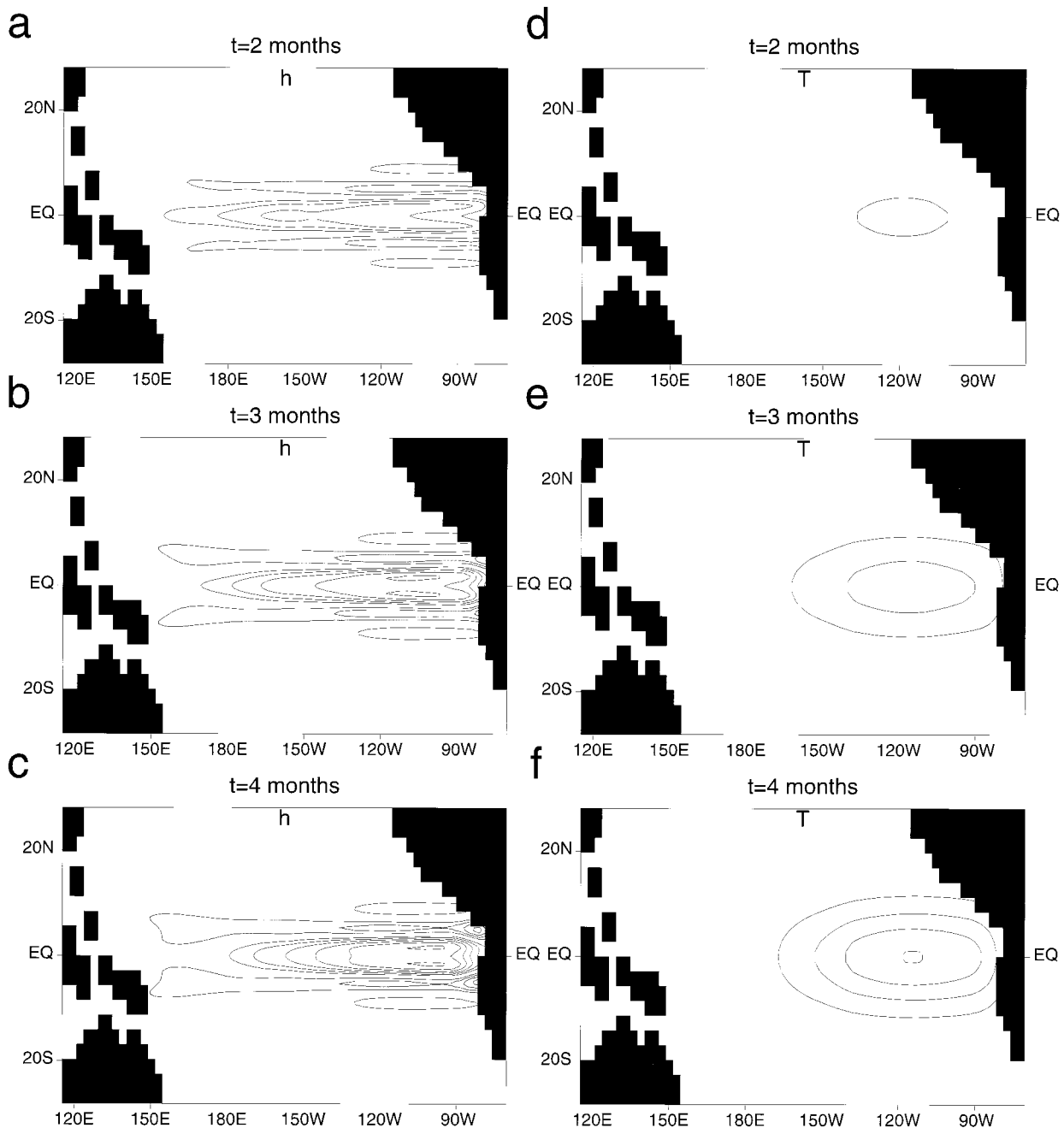

FIG. 11. Same as Fig. 9 but for the case where the coupled model is subjected to only the wind stress component of $\mathbf{S}_1$.

(1996), this can be achieved in that time frame. Perturbations that develop in the late boreal spring and summer, however, have to compete against the westward advance and shrinking of the warm pool creating conditions that are less favorable for perturbation growth. A similar seasonal dependence of optimal perturbation growth rates in the model of Zebiak and Cane (1987) has also been found (Blumenthal 1991; Xue et al. 1994, 1997; Chen et al. 1997).

The mechanism discussed here for seasonal modulation of perturbation growth is distinct from that proposed by Philander et al. (1984) who argued that seasonal variations in the position of atmospheric heating by the mean wind convergence of the intertropical convergence zone (ITCZ) lead to phase-locking of ENSO with the seasonal cycle. The mechanism discussed by Moore and Kleeman (1996) is more similar to that proposed by Hirst (1986) who argued that phase-locking

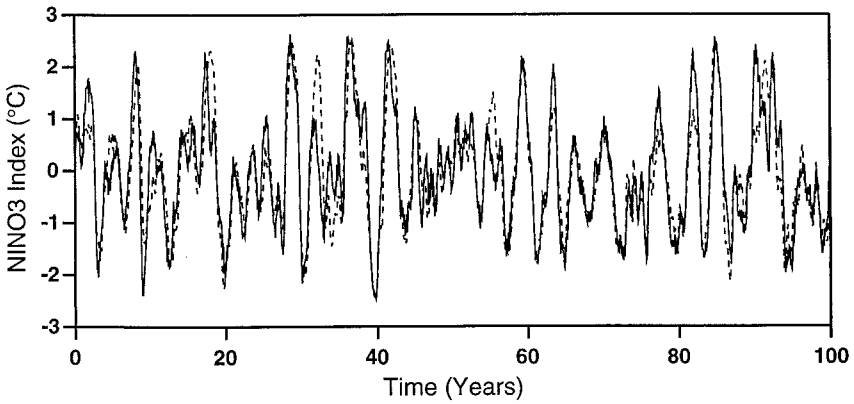

FIG. 12. Time series of the NINO3 index from 100-yr integrations of the coupled model forced with stochastic noise composed of $\mathbf{S}_1$ and $\mathbf{S}_2$. Solid curve shows the case where only the surface heat flux components of $\mathbf{S}_1$ and $\mathbf{S}_2$ are used, and the dashed curve shows the case where only the surface wind stress components are used.

of ENSO was due to seasonal migrations of latent heating over water with SST $>$ 26°C that mirror movements of the ITCZ. However, latent heat release due to deep convection does not occur unless SST $\geq$ 28°C (Graham and Barnett 1987), a condition imposed in the coupled model used here via a moist static energy threshold. Since the 28°C isotherm in the warm pool lies farther to the west than the 26°C isotherm, the growth of perturbations in the Kleeman model is decoupled from movements of the ITCZ, so the mechanism for phase-locking of ENSO discussed above is distinct from that of Hirst (1986) also.

b. The response to combined forcing events

Section 6a indicates that fairly low-amplitude, short-lived convective anomalies and wind anomalies, similar in many respects to those observed in connection with intraseasonal and synoptic variability in the Tropics, can have a significant influence on the ENSO variability of the coupled system. In the model, we can understand the stochastically forced variability in terms of the dynamics of optimal perturbations that have structures very reminiscent of westerly and easterly wind bursts that often occur in association with MJO events (Dunkerton and Crum 1995; Milliff et al. 1998). A westerly wind burst can be spawned in the model by subjecting it to a $-/+$ constant amplitude $\mathbf{S}_1$ forcing for 14 days after which a warm episode develops as shown in section 6a and Fig. 13. In nature, westerly and easterly wind bursts are common over the western tropical Pacific (Madden and Julian 1994), yet ENSO episodes occur much less frequently. It is therefore of interest to examine how wind bursts closely spaced in time with the same or opposite sign influence low-frequency variability. To do this we ran the coupled model starting on 1 January with a $-/+$ constant amplitude $\mathbf{S}_1$ forcing applied during the first 14 days. Immediately following this, a $+/-$ constant amplitude $\mathbf{S}_1$ forcing was applied for the next 14 days. After that, the forcing amplitude was zero. The effects of the $-/+$ forcing are almost completely cancelled out by the $+/-$ forcing, leading to very small SST anomalies as shown in Fig. 13, which shows a time series of the NINO3 index.

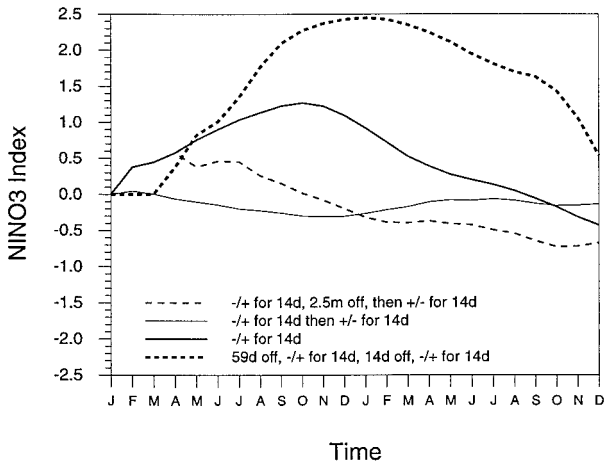

FIG. 13. Time series of the NINO3 index from 2-yr integrations subjected to $\mathbf{S}_1$ forcing fields for the four cases indicated.

To illustrate the effect of ''MJO-like'' events that occur several weeks apart, we ran the coupled model with $-/+$ constant amplitude $\mathbf{S}_1$ forcing during the first 14 days, zero forcing for the next 2.5 months, then with a $+/-$ constant amplitude $\mathbf{S}_1$ forcing for 14 days, then zero forcing for the remainder of the model run. A time series of the resulting NINO3 index is shown in Fig. 13. The warm episode that initially develops in response to $-/+$ is arrested by the $+/-$ forcing that is present 2.5 months later. Evidence for this kind of behavior is apparent in the NINO3 time series in Fig. 2 and in the observed time series. There have also been times in nature when a warm or cold episode never eventuates,

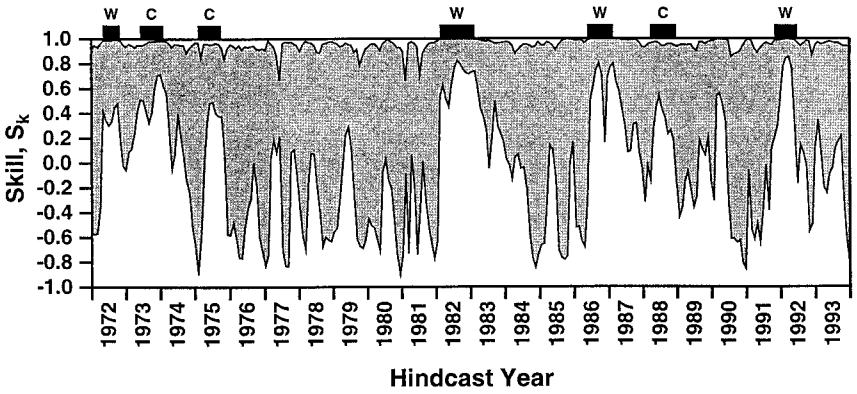

FIG. 14. The envelope defined by the stochastically forced hindcasts of NINO3 index that have the highest and lowest correlations, S_k, with the NINO3 index of the unperturbed hindcast over a 2-yr hindcast period. The timing of the major warm (W) and cold (C) events observed during the period 1972–93 are also indicated.

despite the fact that all of the usual indicators point to an episode occuring.

To illustrate the effect of two MJO-like events of the same sign that occur several weeks apart, we ran the coupled model as follows: 1) zero noise forcing during January and February, 2) $-/+$ constant amplitude $\mathbf{S}_1$ forcing from 1 March to 14 March, 3) zero forcing from 15 March to 31 March, 4) $-/+$ constant amplitude $\mathbf{S}_1$ forcing between 1 April and 14 April, and 5) zero forcing for the remainder of the model run. This scenario is very much like that in the tropical Pacific during 1997 when two strong MJO episodes of the same sign with associated bursts of westerly winds occured during March and April. The resulting NINO3 index from the coupled model is shown in Fig. 13, and in this case a large-amplitude warm episode develops.

The experiments of Fig. 13 also indicate that in the model a predominance of westerly wind bursts over easterly wind bursts will give rise to a warm episode, while a predominance of easterly wind bursts over westerlies will give rise to a cold episode.

c. The importance of nonlinearity

Our experiments illustrate how stochastic noise forcing in the Tropics can disrupt variability on seasonal–interannual timescales in the coupled system, as well as enhance it. The ability of the stochastic forcing to disrupt the system is strongly dependent on the nonlinearities of the coupled model. There are two important nonlinearities in the model associated with 1) an atmospheric moist static energy threshold below which deep penetrative convection anomalies cannot occur, and 2) the depth of the ocean thermocline that does not influence SST anomalies if it is very deep or very shallow. In sequel we will refer to 1 as ''active'' if the moist static energy threshold is exceeded, and 2 as active if the thermocline is very deep or very shallow. As shown by Moore and Kleeman (1996), these nonlinearities can severely inhibit the growth of perturbations in the model. Similar results have been reported by Battisti and Hirst (1989), Chen et al. (1997), and Xue et al. (1997) for the Zebiak and Cane model. The nonlinearity described by 1 is generally active at all times over the west Pacific warm pool, while in the central and eastern Pacific 1 and 2 are typically active only during the development of large-amplitude warm and cold episodes. Therefore, once such an episode is well developed, it is difficult for the noise forcing to disrupt the circulation because noise-induced perturbations cannot grow. To illustrate this, the coupled model was used to hindcast the observed NINO3 index for the period January 1972–December 1993. Two-year hindcasts were started on the first day of each month by spinning up the ocean model for 2 yr with observed wind stress anomalies just prior to coupling with the atmosphere then running the coupled model for 2 yr. As shown by Kleeman et al. (1995), the coupled model demonstrates reasonable skill in predicting trends in the observed NINO3 index during this period. Each of the model hindcasts was repeated 20 times by applying a different realization of the stochastic noise forcing described in section 3. The correlation, S_k, between the NINO3 index of the unperturbed hindcast and each perturbed hindcast was computed over the 2-yr period. Figure 14 shows the envelope defined by the perturbed hindcasts that have the highest and lowest correlations with the unperturbed hindcasts. The width of the envelope at any time is an indication of how effective the noise forcing is at perturbing the coupled system during the following 2-yr period. In general, the envelope is narrow when a large-amplitude warm or cold event is present in the system. It is at these times that the nonlinearities 1 and 2 are most active (see Moore and Kleeman 1996). Note also that some of the model hindcasts incorrectly predict strong ''false'' ENSO episodes (e.g., 1989–90), at which time the nonlinearities 1 and 2 are also active and the envelope is narrow.

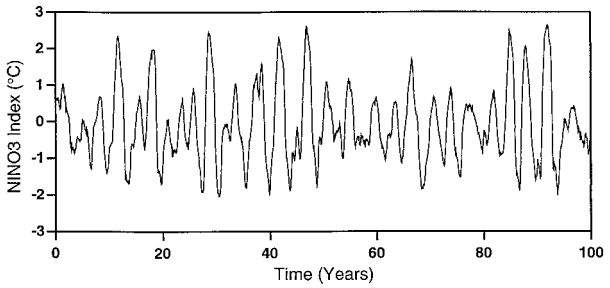

FIG. 15. A time series of the NINO3 index from a 100-yr integration of the coupled model forced with stochastic noise composed of $\mathbf{S}_1$ and $\mathbf{S}_2$. The forcing is applied only during the period Nov–Apr of each year. At all other times of the year, the noise forcing amplitude is zero.

d. Seasonal variations in the noise forcing

Observation shows that MJO is most active during the period November–April. It is of interest, therefore, to see how the stochastically forced coupled system response is influenced by seasonal variations in the stochastic forcing. Figure 15 shows a time series of the NINO3 index from a 100-yr integration of the coupled model forced by stochastic noise as in section 4, but only during the period November–April each year. At all other times of the year, the stochastic forcing amplitude is zero. It would appear that realistic seasonal variations in the level of noise do not alter the ability of the noise to enhance the low-fequency variability of the coupled model. This result can be anticipated from Fig. 8, which shows that the noise is most effective at increasing the coupled system response during the late and early parts of the year.

e. Effects of variations in noise forcing amplitude

The effect of variations in the amplitude of the stochastic forcing on the coupled system response has also been examined. We consider first the case where the model is stable but close to its primary bifurcation point ($\alpha = 6.5$ m s^{-1}, $c_0 = 2.3$ m s^{-1}, and $\gamma = 1.0$). The experiment of section 4 was repeated with the amplitude of the stochastic forcing changed by a factor of $F = 0.5$, $F = 3$, and $F = 5$. The case $F = 0.5$ corresponds to a noise forcing with $\sigma_H = 16.5$ W m^{-2} and $\sigma_W = 0.08$ m s^{-1} in the western tropical Pacific. The case $F = 3$ corresponds to a noise forcing with $\sigma_H = 99$ W m^{-2} and $\sigma_W = 0.48$ m s^{-1} in the western tropical Pacific. The case $F = 5$ corresponds to a noise forcing with $\sigma_H = 165$ W m^{-2} and $\sigma_W = 0.8$ m s^{-1} in western tropical Pacific. Figure 16a shows spectra of the NINO3 index from the case $F = 1$ of section 4, and the cases $F = 0.5$, $F = 3$, and $F = 5$ computed using the maximum entropy method of order 30. Also shown for comparison is the spectrum of the observed NINO3 index. The level of power at the ENSO period agrees best with the observations when $F = 0.5$. As the amplitude of the forcing is increased the power at all frequencies increases, and the spectra tend to become flatter at the low-frequency end, and the agreement between the model and observations deteriorates.

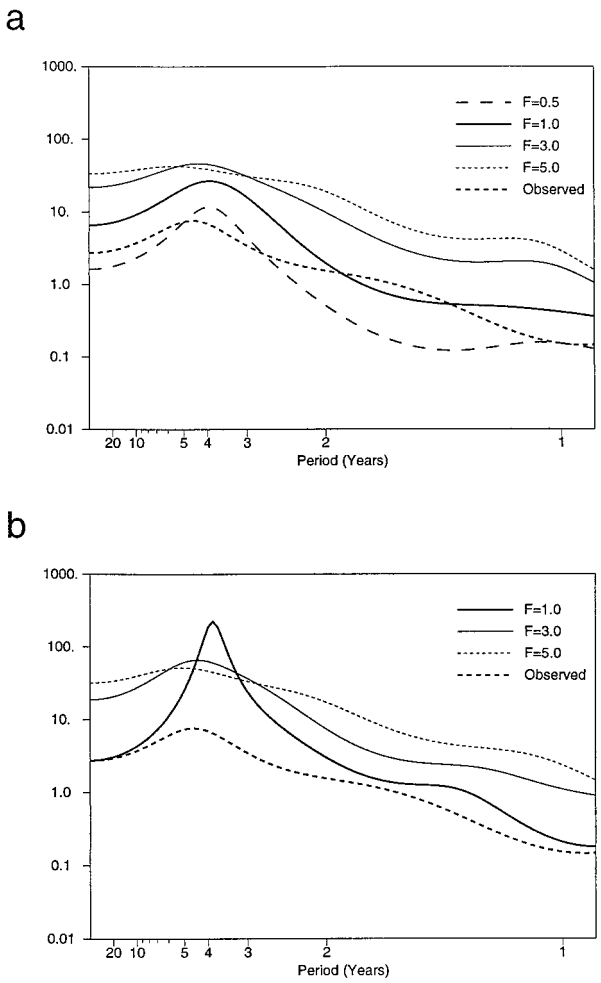

FIG. 16. Power spectra of the NINO3 index from 100-yr integrations of the stochastically forced coupled model. The forcing amplitude is multiplied by the factor F in each case, and the standard case, $F = 1$, corresponds to that discussed in section 4. The cases shown in (a) are from a stable model, while those in (b) are from an unstable model. Also shown is the spectrum of the observed NINO3 index. The spectra were computed using a maximum entropy method of order 30.

Observations indicate that typical MJO related wind anomalies are ~1–3 m s^{-1} in the western tropical Pacific (Hendon and Glick 1997) so $F = 5$ has a wind amplitude approaching the strength of the MJO, yet this case does not agree well with observed spectra. To understand this consider the dynamics of the response of the coupled model to the stochastic forcing described in sections 6a and 6b. It was shown that the stochastic forcing induces in the model perturbations that can undergo rapid growth over periods ranging from a few weeks to a few months and that develop into westerly and easterly wind bursts. Such events are part of the observed intrasea-

sonal variability in nature so one might be tempted to include them as part of the stochastic noise forcing. In the model however, westerly and easterly wind bursts develop from stochastically induced perturbations that grow due to air–sea interaction. Therefore, in the model the noise forcing merely acts to initiate MJO-like events (which cannot develop spontaneously due to the absence of the necessary physics in the model) that develop and amplify via air–sea interaction producing ''wind burst'' structures like those in Fig. 7. The mechanism for this rapid transient growth is discussed by Moore and Kleeman (1996), and is similar to the latent heat-moisture convergence feedback considered by Lau and Shen (1988) and Hirst and Lau (1990).

It is also instructive to consider the effects of an increase in stochastic forcing amplitude in the case where the coupled model is unstable. The parameter choice we have considered in this case is $\alpha = 9$ m s^{-1}, $c_0 = 2.3$ m s^{-1}, and $\gamma = 1.0$. As described above we ran the unstable coupled model subject to stochastic noise with amplitude increased by a factor of $F = 1$, 3, and 5. Figure 16b shows the resulting NIN03 index power spectrum compared to the observed spectrum. When $F = 1$, the noise is ineffective at disrupting the regular, self-sustaining oscillation that is set up in the model (cf Fig. 6), so the spectrum shows a pronounced peak at the frequency of the oscillation. The noise becomes more effective at disrupting the self-sustaining ENSO oscillation as the noise amplitude increases, but the spectrum becomes flatter. The resulting time series of the NINO3 index (not shown) do not look very realistic when compared to the observed time series, which is confirmed by comparing the shape of model and observed spectra in Fig. 16b. The dynamics by which the noise forcing disrupts the self-sustaining oscillation in the unstable model are the same as those described in section 6a and involve disturbances that resemble optimal perturbations. However, as shown in section 6c, the nonlinearties of the model limit the growth of noise-induced perturbations. When the model is unstable, the nonlinearties are active for part of the time during each cycle of the self-sustaining oscillation (Moore and Kleeman 1996), hence noise-induced perturbations are always growth limited, and are relatively ineffective at disrupting the self-sustaining oscillation. Consequently in the unstable case a larger-amplitude forcing is needed to widen the spectral peak of the NINO3 index in Fig. 16 compared to the stable case.

7. Discussion and conclusions

In this paper we have examined the low-frequency response of the coupled ocean–atmosphere system in the tropical Pacific to stochastic forcing in the form of transient activity in the atmosphere and ocean. This was done using an intermediate coupled model of the system and by applying the theoretical ideas of generalized linear stability theory. Using these ideas we have computed the patterns of stochastic noise forcing that produce the largest response in the variability of the coupled system response. These patterns are the so-called stochastic optimals of the the system. The surface heat flux component of the dominant stochastic optimal resembles the latent heating anomalies often observed in association with intraseasonal variability, such as the MJO. The surface wind component of the dominant stochastic optimal takes the form of predominantly zonally orientated wind bands reminiscent of MJO activity and synoptic variability in the real atmosphere (Kleeman and Moore 1997a). Even though the coupled model is stable, when subject to a stochastic noise forcing composed of the dominant stochastic optimals, a very realistic time series of SST anomalies results with a spectrum whose shape compares favorably with the observed variability. A detailed investigation reveals that the stochastic forcing induces perturbations in the coupled system that are favorably configured to grow rapidly. As they develop, these perturbations take the form of westerly and easterly wind bursts in the atmosphere over the western tropical Pacific, and are very effective at generating ENSO epsiodes in the model. It is in this way that the stochastic forcing enhances the variability of the system on seasonal–interannual timescales.

Stochastic forcing in the Tropics enhances seasonal–interannual variability in two ways: 1) by inducing the occurrence of ENSO episodes, and 2) by disrupting developing or existing ENSO episodes. The ability of the noise to achieve these effects depends on a number of factors that include

1) The phase of the seasonal cycle. Perturbations that develop late or early in the year have more of a chance of developing into an ENSO episode by virtue of the seasonal cycle in tropical Pacific SST.
2) The presence of nonlinearities in the system. If the system resides in a nonlinear regime, then the growth of perturbations in generally inhibited. Such regimes include ENSO episodes themselves.
3) The past history of the noise forcing and its integrated effects. If the phase of the noise forcing is continually changing rapidly, then the effect of stochastically induced perturbations of one sign can be arrested by perturbations of the opposite sign that occur soon after. However, if the phase of the stochastic forcing remains constant for a while, or if the amplitude of the noise-induced perturbations varies considerably, then the net effect of the perturbations is a significant change in the seasonal–interannual variabilty of the system. For example, a series of westerly wind bursts closely spaced in time will tend to excite and intensify an El Niño episode, and there is observational evidence for this during ENSO episodes of 1976/77, 1982/83 (Lau and Chan 1988; Luther et al. 1983), 1986/87 (Lau and Chan 1986; 1988), and 1997/98.

By virtue of these factors, the noise forcing can either

spawn new ENSO episodes in the model, or arrest existing episodes before they reach maturity.

The possibility of a connection between variability on intraseasonal timescales and interannual timescales was first suggested by Lau and Chan (1986) and investigated further by Lau and Chan (1988), Lau and Shen (1988), and Hirst and Lau (1990). A number of other studies cited in section 1 have also explored the paradigm that ENSO behaves as a stochastically forced low-frequency oscillation. However, most of these studies have used highly idealized models of ENSO, or have concentrated mainly on the temporal nature of the noise forcing with little regard for the spatial structure of the noise. It is the latter that we have concentrated on here. Based on our work we concur with the investigators cited earlier that ENSO behaves as a stochastically forced phenomena. We have demonstrated that transient wave activity in the atmosphere and ocean, such as intraseasonal variability in the western and eastern tropical Pacific acts as the source of stochastic forcing, exciting perturbations that are favorably configured to undergo rapid transient growth in the form of westerly and easterly wind bursts. Our experiments with a coupled model reveal that decadal variations in ENSO activity in the model can occur quite naturally when viewed in this framework, consistent with the ideas of Hasselmann (1976). The model ENSO is described by a dominant mode of variability of the system, the ''ENSO mode,'' so variability of the system on ENSO timescales depends primarily on time variations in the amplitude of this mode. The amplitude of the ENSO-mode depends on the stochastic forcing, and will be described by a ''random walk,'' so that ENSO variability will be high (low) when the ENSO-mode amplitude is large (small) as shown by Kleeman and Moore (1999). In the cases examined here, spectra of time series agree best with observations when the ENSO mode of the coupled model is stable. This result is somewhat at odds with a recent study by Blanke et al. (1997) who concluded that the ENSO mode may be unstable. However, their conclusions were based on the results of a coupled model and noise forcing fields different to those used in this study. More work with other models along the lines described here is clearly necessary to develop a clearer understanding of these issues.

The ideas presented here have important ramifications for ENSO prediction and predictability and suggest that our ability to predict the onset of ENSO episodes may be limited by our ability to predict the properties and statistics of the stochastic noise forcing. These ideas are currently under investigation using the ensemble prediction techniques of Moore and Kleeman (1998) in which stochastic forcing reminiscent of intraseasonal variability is used to perturb ensemble members. An operational prediction system based on the stochastic nature of ENSO has also been developed by Penland (1996).

The development of the 1997/98 El Niño provides perhaps some direct evidence for the mechanisms discussed in this paper. Just prior to the warming that occurred in the east Pacific, two sizable MJO events passed through the tropical Pacific. Associated with these events were periods of strong westerly wind bursts during March and April that initiated equatorial ocean Kelvin waves with clear signatures in the main ocean thermocline. This chain of events is similar to one of the scenarios described in relation to Fig. 13. Many of the forecasts for ENSO made by various groups around the world prior to the March 1997 wind burst event predicted only a weak warm event. After the wind bursts of March and April however, many of the same models were predicting a much stronger warm event indicating that important precursor signals for the El Niño were not present in the observations used to initialize forecasts prior to March 1997.

While the ideas and mechanisms discussed here are simple, we must not overlook the fact that they have been developed using a simple coupled model, and that there are other physical mechanisms not included in this model that may have a very strong influence on tropical interannual variability. Some of the more obvious factors that we have neglected are 1) changes in the seasonal cycle, and the interaction of the ENSO cycle with the seasonal cycle, 2) effects of interannual variability on intraseasonal variability, 3) the interaction of ENSO with the Indian and Asian monsoons, 4) extratropical influences of the atmospheric and oceanic circulations on the Tropics, 5) interdecadal and intercentennial changes in the ocean thermohaline circulation. Each of these factors are likely to influence the stability of the coupled system in the Tropics and so affect the response of the low-frequency components of the system to the stochastic forcing. Slow variations in the stability of the coupled system are analogous to a slow wandering of the coupled system through parameter space, and as we have demonstrated, this may be another factor contributing to decadal variations in ENSO activity. It would therefore be of interest to repeat the calculations presented here in a hierarchy of coupled models of varying complexity to test the generality of our conclusions. Similarly, a range of other experiments that should certainly be explored also suggest themselves .

A serious limitation of the model used here is the slaved nature of the atmospheric component to the ocean SST. This precludes the development of intrinsic intraseasonal oscillations in the model, as well as the interaction between intraseasonal and interannual oscillations, which is likely to be important (Lau and Chan 1988; Hirst and Lau 1990). This study has been limited to the cases where the stochastic noise forcing is independent of the seasonal–interannual variability of the system. This is probably an oversimplication, and it is likely that in nature the noise forcing is a function of the state of the system. This amounts to replacing $f(t)$ by $f(\Psi, \psi, t)$ in (2) and (3), which is a more complex system, but nonetheless raises some interesting ques-

tions that deserve further investigation, and which will be the subject of future study.

Acknowledgments. AMM gratefully acknowleges partial support by the NOAA Office of Global Programs. We are also grateful to Chris Torrence and Gil Compo as the University of Colorado for their help in performing the wavelet analyses described in the paper. The authors also wish to thank Drs. Cécile Penland, Harry Hendon, and Peter Webster for numerous stimulating discussions on the MJO and the nature of ENSO. The helpful comments and suggestions of two anonymous reviewers are also gratefully acknowledged.

REFERENCES

Battisti, D. S., 1988: Dynamics and thermodynamics of a warming event in a coupled tropical atmosphere–ocean model. *J. Atmos. Sci.,* **45,** 2889–2919.

——, and A. C. Hirst, 1989: Interannual variability in the tropical atmosphere–ocean system: Influence of the basic state, ocean geometry, and nonlinearity. *J. Atmos. Sci.,* **46,** 1687–1712.

——, and E. S. Sarachik, 1995: Understanding and predicting ENSO. *Rev. Geophys.,* (Suppl.), 1367–1376.

Blanke, B., J. D. Neelin, and D. Gutzler, 1997: Estimating the effect of stochastic wind stress forcing on ENSO irregularity. *J. Climate,* **10,** 1473–1486.

Blumenthal, M. B., 1991: Predictability of a coupled ocean–atmosphere model. *J. Climate,* **4,** 766–784.

Boulanger, J.-P., and L.-L. Fu, 1996: Evidence of boundary reflection of kelvin and first-mode Rossby waves from TOPEX/POSEIDON sea level data. *J. Geophys. Res.,* **101,** 16 361–16 371.

Chang, P., B. Wang, T. Li, and L. Ji, 1994: Interactions between the seasonal cycle and ENSO-frequency entrainment and chaos in a coupled atmosphere–ocean model. *Geophys. Res. Lett.,* **21,** 2817–2820.

Chen, Y.-Q., D. S. Battisti, T. N. Palmer, J. Barsugli, and E. S. Sarachik, 1997: A study of the predictability of tropical Pacific SST in a coupled atmosphere/ocean model using singular vector analysis: The role of the annual cycle and the ENSO cycle. *Mon. Wea. Rev.,* **125,** 831–845.

Davey, M. K., and A. E. Gill, 1987: Experiments on tropical circulation with a moist model. *Quart. J. Roy. Meteor. Soc.,* **113,** 1237–1270.

Dunkerton, T. J., and F. X. Crum, 1995: Eastward propagating ~2- to 15-day equatorial convection and its relation to the tropical intraseasonal oscillation. *J. Geophys. Res.,* **100,** 25 781–25 790.

Eckert, C., and M. Latif, 1997: Predictability of a stochastically forced hybrid coupled model of El Niño. *J. Climate,* **10,** 1488–1504.

Emmanuel, K. A., 1987: An air–sea interaction model of intraseasonal oscillations in the tropics. *J. Atmos. Sci.,* **44,** 2324–2340.

Farrell, B. F., 1985: Transient growth of baroclinic waves. *J. Atmos. Sci.,* **42,** 2718–2727.

——, 1989: Optimal excitation of baroclinic waves. *J. Atmos. Sci.,* **46,** 1193–1206.

——, and P. J. Ioannou, 1996a: Generalized stability theory. Part I: Autonomous operators. *J. Atmos. Sci.,* **53,** 2025–2040.

——, and ——, 1996b: Generalized stability theory. Part II: Nonautonomous operators. *J. Atmos. Sci.,* **53,** 2041–2053.

Gill, A. E., 1980: Some simple solutions for heat-induced tropical circulation. *Quart. J. Roy. Meteor. Soc.,* **106,** 447–462.

——, 1985: Elements of coupled ocean–atmosphere models for the Tropics. *Coupled Ocean–Atmosphere Models,* J. C. J. Nihoul, Ed., Elsevier, 303–327.

Graham, N., and T. P. Barnett, 1987: Observations of sea surface temperature and convection over tropical oceans. *Science,* **238,** 657–659.

Gray, W. M., and J. D. Sheaffer, 1997: The Atlantic Ocean thermohaline circulation as a flywheel for multi-decadal global and regional climate changes. *Proc. Seventh Conf. on Climate Variations,* Long Beach, CA, Amer. Meteor. Soc., 313–318.

Gu, D., and S. G. H. Philander, 1997: Interdecadal climate fluctuations that depend on exchanges between the Tropics and extratropics. *Science,* **265,** 805–807.

Hasselmann, K., 1976: Stochastic climate models. Part I: Theory. *Tellus,* **28,** 289–305.

Hendon, H. H., and J. Glick, 1997: Intraseasonal air–sea interaction in the tropical Indian and Pacific Oceans. *J. Climate,* **10,** 647–661.

Hirst, A. C., and K.-M. Lau, 1990: Intraseasonal and interannual oscillations in coupled ocean–atmosphere model. *J. Climate,* **3,** 713–725.

Jin, F.-F., 1997: An equatorial ocean recharge paradigm for ENSO Part I: Conceptual model. *J. Atmos. Sci.,* **54,** 811–829.

——, J. D. Neelin, and M. Ghil, 1994: El Niño on the Devil's Staircase: Annual subharmonic steps to chaos. *Science,* **264,** 70–72.

——, ——, and ——, 1996: El Niño–Southern Oscillation and the annual cycle: Subharmonic frequency locking and aperiodicity. *Physica D,* **9,** 442–465.

Jones, C., and B. C. Weare, 1996: On the relationship between low-frequency variability in latent heat fluxes over the tropical oceans and the Madden–Julian oscillation. *J. Climate,* **9,** 3086–3104.

Kestin, T. S., D. J. Karoly, J.-I. Yano, and N. A. Rayner, 1998: Time–frequency variability of ENSO and stochastic simulations. *J. Climate,* **11,** 2258–2272.

Kleeman, R., 1989: A modeling study of the effect of the Andean Mountains on the summertime circulation of tropical South America. *J. Atmos. Sci.,* **46,** 3344–3362.

——, 1991: A simple model of the atmospheric response to ENSO sea surface temperature anomalies. *J. Atmos. Sci.,* **48,** 3–18.

——, 1993: On the dependence of hindcast skill on ocean thermodynamics in a coupled ocean–atmosphere model. *J. Climate,* **6,** 2012–2033.

——, 1994: Forecasts of tropical Pacific SST using a low-order coupled ocean–atmosphere dynamical model. NOAA Experimental Long-Lead Forecast Bulletin. [Available from NOAA Climate Prediction Center, 5200 Auth Rd., Washington, DC 20333.]

——, and A. M. Moore, 1997: A theory for the limitations of ENSO predictability due to stochastic atmospheric transients. *J. Atmos. Sci.,* **54,** 753–767.

——, and ——, 1998: A new method for determining the reliability of dynamical ENSO predictions. *Mon. Wea. Rev.,* **127,** 694–705.

——, M. Latif, and M. Flügel, 1992: A hybrid tropical atmosphere ocean model: Sensitivities and hindcast skill. Max-Planck Institut für Meteorologie Rep. 76, 37 pp.

——, ——, and N. R. Smith, 1995: Assimilation of subsurface thermal data into an intermediate tropical coupled ocean–atmosphere model. *Mon. Wea. Rev.,* **123,** 3103–3113.

Kloeden, P. E., and E. Platen, 1992: *Numerical Solution of Stochastic Differential Equations.* Springer-Verlag, 632 pp.

Krishnamurti, T. N., D. K. Oosterhof, and A. V. Mehta, 1988: Air–sea interaction on the timescale of 30–50 days. *J. Atmos. Sci.,* **45,** 1304–1322.

Lau, K.-M., 1985: Elements of a stochastic dynamical theory of the long-term variability of the El Niño–Southern Oscillation. *J. Atmos. Sci.,* **42,** 1552–1558.

——, and P. H. Chan, 1985: Aspects of the 40–50 day oscillation during the northern winter as inferred from outgoing longwave radiation. *Mon. Wea. Rev.,* **113,** 1889–1909.

——, and ——, 1986: The 40–50 day oscillation and the El Nino–Southern Oscilation: A new perspective. *Bull. Amer. Meteor. Soc.,* **67,** 533–534.

——, and ——, 1988: Intraseasonal and interannual variations of tropical convection: A possible link between 40–50 day oscillation and ENSO? *J. Atmos. Sci.,* **45,** 506–521.

——, and S. Shen, 1988: On the dynamics of intraseasonal oscillations and ENSO. *J. Atmos. Sci.,* **45,** 1781–1797.

Liu, Z., S. G. H. Philander, and R. C. Pacanowski, 1994: A GCM study of tropical–subtropical upper-ocean water exchange. *J. Phys. Oceanogr.,* **24,** 2606–2623.

Luther, D. S., D. E. Harrison, and R. A. Knox. 1983: Zonal winds in the central equatorial Pacific and El Niño. *Science,* **222,** 327–330.

Madden, R. A., and P. R. Julian, 1994: Observations of the 40–50-day tropical oscillation—A review. *Mon. Wea. Rev.,* **122,** 814–837.

Mantua, N. J., and D. S. Battisti, 1994: Evidence for the delayed oscillator mechanism for ENSO: The ''observed'' oceanic Kelvin mode in the far western Pacific. *J. Phys. Oceanogr.,* **24,** 691–699.

McCreary, J. P., 1983: A model of tropical ocean–atmosphere interaction. *Mon. Wea. Rev.,* **111,** 370–387.

——, and D. L. T. Anderson, 1991: An overview of coupled ocean–atmosphere models of El Niño and the Southern Oscillation. *J. Geophys. Res.,* **96,** 3125–3150.

——, and P. Lu, 1994: Interaction between the subtropical and equatorial ocean circulations: The subtropical cell. *J. Phys. Oceanogr.,* **24,** 466–497.

Meyers, S. D., B. G. Kelly, and J. J. O'Brien, 1993: An introduction to wavelet analysis in oceanography and meteorology: With application to the dispersion of Yanai waves. *Mon. Wea. Rev.,* **121,** 2858–2866.

Milliff, R. F., T. J. Hoar, and R. A. Madden, 1998: Fast, eastward-moving disturbances in the surface winds of the equatorial Pacific. *Tellus,* **50A,** 26–41.

Moore, A. M., and R. Kleeman, 1996: The dynamics of error growth and predictability in a coupled model of ENSO. *Quart. J. Roy. Meteor. Soc.,* **122,** 1405–1446.

——, and ——, 1997a: The singular vectors of a coupled ocean–atmosphere model of ENSO. Part I: Thermodynamics, energetics and error growth. *Quart. J. Roy. Meteor. Soc.,* **123,** 953–981.

——, and ——, 1997b: The singular vectors of a coupled ocean–atmosphere model of ENSO. Part II: Sensitivity studies and dynamical interpretation *Quart. J. Roy. Meteor. Soc.,* **123,** 983–1006.

——, and ——, 1998: Skill assessment for ENSO using ensemble prediction. *Quart. J. Roy. Meteor. Soc.,* **124,** 557–584.

——, and ——, 1999: The non-normal nature of El Niño and intraseasonal variability. *J. Climate,* in press.

Munnich, M., M. A. Cane, and S. E. Zebiak, 1991: A study of self-excited oscillations in the tropical ocean–atmosphere system: Part II. Nonlinear cases. *J. Atmos. Sci.,* **48,** 1238–1248.

National Research Council, 1996: *Learning to Predict Climate Variations Associated with El Niño and the Southern Oscillation: Accomplishments and Legacies of the TOGA Program.* National Research Council, 171 pp.

Neelin, J. D., 1990: A hybrid coupled general circulation model for El Niño studies. *J. Atmos. Sci.,* **47,** 674–693.

——, 1991: The slow sea surface temperature mode and the fast-wave limit: Analytic theory for tropical interannual oscilations and experiments in a hybrid coupled model. *J. Atmos. Sci.,* **48,** 584–606.

——, I. M. Held, and K. H. Cook, 1987: Evaporation wind-feedback and low-frequency variability in the tropical atmosphere. *J. Atmos. Sci.,* **44,** 2341–2348.

——, M. Latif, and F.-F. Jin, 1994: Dynamics of coupled ocean–atmosphere models: The tropical problem. *Annu. Rev. Fluid Mech.,* **26,** 617–659.

Penland, C., 1996: A stochastic model of IndoPacific sea surface temperature anomalies. *Physica D,* **98,** 534–558.

——, and L. Matrasova, 1994: A balance condition for stochastic numerical models with application to El Niño–Southern Oscillation. *J. Climate,* **7,** 1352–1372.

——, and P. D. Sardeshmukh, 1995: The optimal growth of tropical sea surface temperature anomalies. *J. Climate,* **8,** 1999–2024.

Philander, S. G. H., T. Yamagata, and R. C. Pacanowski, 1984: Unstable air–sea interactions in the tropics. *J. Atmos. Sci.,* **41,** 604–613.

Picaut, J., M. Ioualalen, C. Menkes, T. Delcroix, and M. J. McPhaden, 1996: Mechanisms of the zonal displacements of the Pacific warm pool: Implications for ENSO. *Science,* **274,** 1486–1489.

Press, W. H., S. A. Teukolsky, W. T. Vetterling, and B. P. Flannery, 1996: *Numerical Recipes in Fortran 77: The Art of Scientific Computing.* 2d ed. Cambridge University Press, 933 pp.

Rasmusson, E. M., and T. H. Carpenter, 1982: Variations in tropical sea surface temperature and surface winds associated with the Southern Oscillation–El Niño. *Mon. Wea. Rev.,* **110,** 354–384.

Schopf, P. S., and M. J. Suarez, 1988: Vacillations in a coupled ocean–atmosphere model. *J. Atmos. Sci.,* **45,** 549–566.

Sperber, K. R., J. M. Slingo, P. M. Inness, and K.-M. Lau, 1997: On the maintenance and initiation of the intraseasonal oscillation in the NCEP/NCAR reanalysis and in the GLA and UKMO AMIP simulations. *Climate Dyn.,* **13**, 769–795.

Suarez, M. J., and P. S. Schopf, 1988: A delayed action oscillator for ENSO. *J. Atmos. Sci.,* **45,** 3283–3287.

Torrence, C., and P. J. Webster, 1998: The annual cycle of persistence in the El Niño–Southern Oscillation. *Quart. J. Roy. Meteor. Soc.,* **124,** 1985–2004.

——, and G. P. Compo, 1998: A practical guide to wavelet analysis. *Bull. Amer. Meteor. Soc.,* **79,** 61–78.

Tziperman, E., L. Stone, M. A. Cane, and H. Jarosh, 1994: El Niño chaos: Overlapping of resonances between the seasonal cycle and the Pacific ocean–atmosphere oscillator. *Science,* **264,** 72–74.

——, M. A. Cane, and S. E. Zebiak, 1995: Irregularity and locking to the seasonal cycle in an ENSO prediction model as explained by the quasi-periodicity route to chaos. *J. Atmos. Sci.,* **52,** 293–306.

——, S. E. Zebiak, and M. A. Cane, 1997: Mechanisms of seasonal–ENSO interaction. *J. Atmos. Sci.,* **54,** 61–71.

Vallis, G. K., 1988: Conceptual models of El Niño and the Southern Oscillation. *J. Geophys. Res.,* **93,** 13 979–13 991.

Wainer, I., and P. J. Webster, 1996: Monsoon/El Nino–Southern Oscillation relationships in a simple coupled ocean–atmosphere model. *J. Geophys. Res.,* **101,** 25 599–25 614.

Xue, Y., M. A. Cane, S. E. Zebiak, and M. B. Blumenthal, 1994: On the prediction of ENSO: A study with a low order Markov model. *Tellus,* **46A,** 512–528.

——, ——, and ——, 1997: Predictability of a coupled model of ENSO using singular vector analysis. Part I: Optimal growth in seasonal background and ENSO cycles. *Mon. Wea. Rev.,* **125,** 2043–2056.

Zebiak, S. E., 1989: On the 30–60 day oscillation and the prediction of El Niño. *J. Climate,* **2,** 1381–1387.

——, and M. A. Cane, 1987: A model of El Niño–Southern Oscillation. *Mon. Wea. Rev.,* **115,** 2262–2278.

——, and ——, 1991: Natural climate variability in a coupled model. *Greenhouse Gas Induced Climate Change,* M. E. Schlesinger, Ed., Elsevier, 457–470.